

1 Overview: Fusion of Radar Polarimetry and Numerical Atmospheric 2 Modelling Towards an Improved Understanding of Cloud and 3 Precipitation Processes

4 Silke Trömel^{1,2}, Clemens Simmer¹, Ulrich Blahak³, Armin Blanke¹, Sabine Doktorowski⁴, Florian
5 Ewald⁵, Michael Frech⁶, Mathias Gergely⁶, Martin Hagen⁵, Tijana Janjic⁷, Heike Kalesse-Los⁶, Stefan
6 Kneifel⁸, Christoph Knote^{7,9}, Jana Mendrok³, Manuel Moser^{10,5}, Gregor Köcher⁷, Kai Mühlbauer¹,
7 Alexander Myagkov¹¹, Velibor Pejdic¹, Patric Seifert¹², Prabhakar Shrestha¹, Audrey Teisseire¹², Leonie
8 von Terzi⁸, Eleni Tetoni⁵, Teresa Vogl⁴, Christiane Voigt^{10,5}, Yuefei Zeng⁷, Tobias Zinner⁷, Johannes
9 Quaas⁴

10 ¹Institute for Geosciences, Department of Meteorology, University of Bonn, Bonn, 53121, Germany

11 ²Laboratory for Clouds and Precipitation Exploration, Geoverbund ABC/J, Bonn, 53121, Germany

12 ³Deutscher Wetterdienst (DWD), Offenbach, 63067, Germany

13 ⁴Institute for Meteorology, Universität Leipzig, Leipzig, 04103, Germany

14 ⁵Institute for Physics of the Atmosphere, DLR, Oberpfaffenhofen, 82234, Germany

15 ⁶Deutscher Wetterdienst (DWD), Observatorium Hohenpeißenberg, Hohenpeißenberg, 82383, Germany

16 ⁷Meteorological Institute Munich, Ludwig-Maximilians-Universität München, 80333, Germany

17 ⁸Institute of Geophysics and Meteorology, University of Cologne, 50969, Germany

18 ⁹Faculty of Medicine, University of Augsburg, Augsburg, 86159 Germany

19 ¹⁰Institute for Physics of the Atmosphere, University Mainz, Mainz, 55099, Germany

20 ¹¹Radiometer Physics GmbH, Meckenheim, 53340, Germany

21 ¹²Leibniz Institute for Tropospheric Research (TROPOS), 04318 Leipzig, Germany

22
23
24 *Correspondence to:* Silke Trömel (silke.troemel@uni-bonn.de)

25 **Abstract.** Cloud and precipitation processes are still a main source of uncertainties in numerical weather prediction and climate
26 change projections. The Priority Program “Polarimetric Radar Observations meet Atmospheric Modelling (PROM)“, funded
27 by the German Research Foundation (Deutsche Forschungsgemeinschaft, DFG), is guided by the hypothesis that many
28 uncertainties relate to the lack of observations suitable to challenge the representation of cloud and precipitation processes in
29 atmospheric models. Such observations can, however, at present be provided e.g. by the recently installed dual-polarization
30 C-band weather radar network of the German national meteorological service in synergy with cloud radars and other
31 instruments at German supersites and similar national networks increasingly available worldwide. While polarimetric radars
32 potentially provide valuable in-cloud information e.g. on hydrometeor type, quantity, and microphysical cloud and
33 precipitation processes, and atmospheric models employ increasingly complex microphysical modules, considerable

34 knowledge gaps still exist in the interpretation of the observations and in the optimal microphysics model process formulations.
35 PROM is a coordinated interdisciplinary effort to increase the use of polarimetric radar observations in data assimilation, which
36 requires a thorough evaluation and improvement of parameterizations of moist processes in atmospheric models. As an
37 overview article of the inter-journal special issue “Fusion of radar polarimetry and numerical atmospheric modelling towards
38 an improved understanding of cloud and precipitation processes”, this article outlines the knowledge achieved in PROM during
39 the past two years and gives perspectives for the next four years.

40 **1 Introduction and Objectives of the priority program**

41 Among the main sources of uncertainty in the models used in numerical weather prediction (NWP) and climate change
42 projections are the parameterizations of cloud and precipitation processes (Bauer et al., 2015). A major part of these
43 uncertainties can be attributed to missing observations suitable to challenge the representation of cloud and precipitation
44 processes employed in atmospheric models. A wealth of new information on precipitation microphysics and generating
45 processes can be gained from observations from polarimetric weather radars and their synergistic analysis at different
46 frequencies. The dual-polarization upgrade of the United States National Weather Service (NWS) S-band Weather
47 Surveillance Radar 1988 Doppler (WSR-88D) network was completed in 2013. Germany finished upgrading its C-band
48 network to polarimetry in 2015 in parallel with other European countries. The synergistic exploitation of polarimetric
49 precipitation radars together with measurements from cloud radars and other instrumentation available at supersites and
50 research institutions enables for the first time a thorough evaluation and potential improvement of current microphysical
51 parameterizations based on detailed multi-frequency remote-sensing observations. Data assimilation merges observations and
52 models for state estimation as a prerequisite for prediction and can be seen as a smart interpolation between observations while
53 exploiting the physical consistency of atmospheric models as mathematical constraint.

54 Considerable knowledge gaps still exist, however, both in radar polarimetry and atmospheric models, which still impede the
55 full exploitation of the triangle between radar polarimetry, atmospheric models, and data assimilation and call for a coordinated
56 interdisciplinary effort. The German Research Foundation (Deutsche Forschungsgemeinschaft, DFG) responded to this call
57 and established the Priority Program “Polarimetric Radar Observations meet Atmospheric Modelling (PROM)”; its first 3-
58 year funding period began in 2019, which will be followed by a second funding period starting in 2022. PROM exploits the
59 synergy of polarimetric radar observations and state-of-the-art atmospheric models to better understand moist processes in the
60 atmosphere, and to improve their representation in climate- and weather prediction models. The overarching goal is to extend
61 our scientific understanding at the verges of the three disciplines, radar polarimetry – atmospheric models – data assimilation,
62 for better predictions of precipitating cloud systems. To approach this goal the initiators of PROM at the Universities of Bonn
63 and Leipzig in Germany identified the following five objectives (see also Trömel et al., 2018):

- 64 1) Exploitation of radar polarimetry for quantitative process detection in precipitating clouds and for model evaluation
65 including a quantitative analysis of polarimetric fingerprints and microphysical retrievals,
- 66 2) improvement of cloud and precipitation schemes in atmospheric models based on process fingerprints detectable in
67 polarimetric observations,
- 68 3) monitoring of the energy budget evolution due to phase changes in the cloudy, precipitating atmosphere for a better
69 understanding of its dynamics,
- 70 4) analyzing precipitation system by assimilation of polarimetric radar observations into atmospheric models for weather
71 forecasting, and
- 72 5) radar-based detection of the initiation of convection for the improvement of thunderstorm prediction.

73 In the first funding period, each of the 14 projects (see <https://www2.meteo.uni-bonn.de/spp2115>) distributed over Germany
74 contribute to at least one of these objectives. In most projects, a radar meteorologist works together with a modeller in order
75 to successfully combine expert knowledge from both research fields. This overview article of the ACP/AMT/GMD inter-
76 journal special issue entitled "Fusion of radar polarimetry and numerical atmospheric modelling towards an improved
77 understanding of cloud and precipitation processes" outlines methodologies developed and results achieved from a selection
78 of the projects during the past two years, and provides overall perspectives for the next four years. The paper is organized as
79 follows: Section 2 explains prevailing challenges in the representation of clouds in atmospheric models, while Sect. 3 provides
80 methodologies to extend our insight in the microphysics of clouds and precipitation by exploiting radar polarimetry. Section 4
81 addresses the fusion of numerical modelling and radar polarimetry via model evaluation either in radar observation space using
82 observation operators or using microphysical retrievals. First conclusions for improved model parameterizations and for a
83 better representation of model uncertainty in radar data assimilation are drawn. Section 5 provides a summary and perspectives
84 for the following years.

85 **2 Representation of clouds in atmospheric models**

86 The representation of cloud and precipitation processes in atmospheric models is a central challenge for NWP and climate
87 projections (e.g., Bauer et al., 2015; Forster et al., 2021), which also impacts offline hydrological models by modulating the
88 distribution of incoming solar radiation and precipitation and affecting the simulated hydrological processes such as
89 evapotranspiration, runoff, and groundwater depths (e.g., Shrestha, 2021). While the primitive equations provide a solid
90 theoretical basis for atmospheric model dynamics, the key diabatic processes that drive energetics and thus circulation, are
91 poorly resolved. Important diabatic processes are linked to cloud and precipitation microphysics acting at scales of micrometres
92 and turbulent processes ranging from several to hundreds of meters. While significant progress has been achieved by high-
93 resolution modelling at the coarser end of this range (e.g., Heinze et al., 2017; Stevens et al., 2020), the intricate and complex
94 microphysical processes still require parameterizations in any dynamic atmospheric model down to and including the scale of
95 direct numerical simulations (e.g., Mellado et al., 2009).

96 A key uncertainty in weather prediction and climate modelling results from the still-rudimentary representation of moist
97 processes and from the diabatic heating/cooling the models induce due to latent heat and their interaction with radiation. The
98 generation and interpretation of past and future climate states additionally has to consider changes in microphysical processes
99 due to anthropogenic aerosol acting, e.g., as cloud condensation nuclei and ice nucleating particles. For short-term weather
100 prediction, the location and evolution of convective events with lifetimes of hours or less are particularly challenging, while
101 relatively slow moving and frontal systems with lifetimes of days show reasonable predictability (Alifieri et al., 2012).

102 Atmospheric modelling in Germany has recently seen substantial advances both in terms of cloud-resolving simulations in
103 NWP mode and in the implementation of ice and mixed-phase precipitation formation processes. Traditionally, different model
104 systems were used for NWP and climate modelling, which were also both heavily used in academic research. The modelling
105 system for long-term climate integrations is the ECHAM model (Stevens et al., 2013). Since it was created by modifying
106 global forecast models developed by ECMWF (European Centre for Medium-Range Weather Forecasts), its name is a
107 combination of ECMWF and Hamburg, the place of development of its parameterization package. The COSMO model,
108 however, was operated at horizontal resolutions down to 2.8 km and used for NWP and reanalysis studies. Both model families
109 are currently being replaced by the ICOSahedral Nonhydrostatic (ICON) modelling framework (Zängl et al., 2015) jointly
110 developed by the Max-Planck Institute for Meteorology and the German national meteorological service (Deutscher
111 Wetterdienst, DWD). Its climate version (the ICON general circulation model, ICON GCM) inherited its physics package
112 from the ECHAM model, and the NWP version incorporated the one from the COSMO model. A third version largely based
113 on the COSMO physics package was developed for higher resolutions (Dipankar et al., 2015) and employs a large-eddy
114 turbulence scheme (ICON-LEM). The latter is able to operate on large domains (Heinze et al., 2017; Stevens et al., 2020) and
115 includes aerosol-cloud interactions (Costa-Surós et al., 2020). In PROM primarily the three ICON model variants (ICON-
116 LEM, ICON-NWP, and ICON-A/GCM) are used.

117 In most atmospheric models, cloud and precipitation microphysical processes are represented by bulk microphysical schemes
118 that distinguish between different hydrometeor classes and include their specific masses as prognostic variables while their
119 size distributions are parameterized (the ICON model considered here uses the scheme by Seifert and Beheng, 2006).
120 Computationally much more demanding are so-called spectral-bin microphysics schemes (Khain et al., 2015), which evolve
121 cloud- and precipitation particle size distributions discretized into size-interval bins. An example is the Hebrew University
122 Cloud Model (HUCM) created by Khain et al. (2005) that treats both liquid and much more intricate (since ice may occur in
123 various shapes and densities) ice crystal distributions. The model is employed by some of the PROM projects in addition to
124 the liquid-only bin-microphysics model by Simmel et al. (2015) extended to the ice phase based on the scheme by Hashino
125 and Tripoli (2007). For the simulation of the evolution of specific air volumes a Lagrangian particle model (McSnow; Brdar
126 and Seifert, 2018) is used in PROM, that models ice and mixed-phase microphysical processes such as depositional growth,
127 aggregation, riming, secondary ice generation, and melting closer to the real processes than bulk formulations. Microphysical

128 processes including radiation-particle interactions obviously depend on particle shape; thus, the evolution of shapes in particle
129 models – and their signatures in radar observations – is instrumental for a full understanding and adequate representation of
130 the microphysical processes in models. Advanced microphysical parameterizations such as spectral-bin or Lagrangian particle
131 schemes are relevant for cloud-resolving models and exploited in PROM for the development and improvement of bulk
132 parameterizations. Scientific questions about global climate require long model integrations and thus coarse spatial resolutions
133 due to computing time constraints. At these resolutions (usually of order of $100 \times 100 \text{ km}^2$ in the horizontal), fractional
134 cloudiness needs to be considered when the grid-box mean relative humidity is below 100%, which requires parameterizations
135 of subgrid-scale variability in relative humidity. Here, PROM builds on assumptions employed in the global ICON model
136 (ICON GCM) to predict fractional cloudiness (e.g., Quaas, 2012).

137 **3 Observational insights from polarimetric radar observations and challenges**

138 DWD operates 17 state-of-the-art polarimetric Doppler C-band weather radars which provide a 3-D sampling of precipitating
139 particles above Germany every five minutes. Together with their Doppler information, radars are the backbone for precipitation
140 and nowcasting products for all meteorological services. Although precipitation monitoring is still the most widespread
141 application of weather radars, their upgrade to polarimetry worldwide not only improves precipitation estimates; their
142 observations are also increasingly exploited for the evaluation and improvement of the representation of cloud- and
143 precipitation processes in atmospheric models (e.g., Gao et al., 2011; Jung et al., 2012; You et al., 2020; Wang et al., 2020).
144 Additional observations from cloud radars available at so-called supersites (in Germany e.g., the Jülich Observatory for Cloud
145 Evolution – Core Facility; JOYCE-CF; Löhnert et al., 2015; <http://www.cpex-lab.de>), universities, and research facilities (e.g.
146 the Leipzig Aerosol and Cloud Remote Observations System; LACROS; Bühl et al., 2013) open opportunities to inform and
147 improve atmospheric models. The use of shorter wavelengths of cloud radars shifts the sensitivity of the observations towards
148 smaller particles and partly increases the magnitude of the received polarimetric signals (e.g. K_{DP} – the differential phase shift
149 between horizontal and vertical polarization per distance called specific differential phase – scales with λ^{-1}), which allows for
150 more detailed studies of ice and cloud microphysics. Polarimetric and multi-frequency radar observations allow for a more
151 granular look at microphysical processes and provide a great data base for model evaluation, the improvement of microphysical
152 parameterizations, and data assimilation, and thus have the potential to significantly improve both weather forecasts and
153 climate predictions.

154 **3.1 Multi-frequency and spectral polarimetry for ice and cloud microphysics**

155 The PROM-project *Understanding Ice Microphysical Processes by combining multi-frequency and spectral Radar*
156 *polarImetry aNd super-parTicle modelling (IMPRINT)* improves ice microphysical process understanding by using spectral
157 multi-frequency and radar polarimetric observations in combination with Monte-Carlo Lagrangian super-particle modeling
158 (Brdar and Seifert, 2018). Mid-latitude stratiform clouds, which occur frequently during winter time over JOYCE-CF, are the

159 main focus. Radar polarimetric variables are well known to be particularly sensitive to the presence of asymmetric ice particles
160 (e.g. Kumjian, 2013). Only recently, also polarimetric cloud radars operating at Ka or W-band are routinely available (Oue et
161 al., 2018; Myagkov et al., 2016; Bühl et al., 2016; Matrosov et al., 2012). Some polarimetric variables are wavelength
162 dependent (K_{DP} is inversely proportional to the wavelength), which provides enhanced sensitivity to ice particle concentration
163 at higher frequencies. Multi-frequency approaches are complementary to radar polarimetry as they are sensitive to larger ice
164 particles. Most commonly, the dual wavelength ratio (DWR), defined as the logarithmic difference of the effective reflectivity
165 Z_e at two frequencies, is used. When ice particles transition from Rayleigh into non-Rayleigh scattering from one wavelength
166 to a higher one, the DWR increases, which allows inferring the characteristic size of the underlying size distribution. The use
167 of three radar frequencies (e.g. X, Ka, W) extends the discernable size range; e.g. the DWR of the Ka-W combination saturates
168 for very large particles (Kneifel et al., 2015; Ori et al., 2021). The information content can be further extended when also the
169 Doppler spectral information is explored. The different fall velocities allow for the separation of different hydrometeors; the
170 high differential reflectivity (Z_{DR}) signal originating from small, slow falling ice crystals can be distinguished from the also
171 low Z_{DR} signal of faster falling snow aggregates, which usually dominate the total Z_{DR} . Only few studies used so far spectral
172 polarimetric observations for ice and snow microphysical studies (Luke et al., 2021; Oue et al., 2018; Pfitzenmayer et al.,
173 2018; Spek et al., 2008). The observations collected during the first multi-months winter campaign carried out at JOYCE-CF
174 as part of the IMPRINT project provide for the first time the opportunity to investigate both, polarimetry and multi-frequency
175 observations in the Doppler spectra space. An example is the analysis of the dendritic growth layer (DGL) illustrated in Fig. 1
176 for a snowfall event observed on 22 January 2019 at JOYCE-CF. Especially in the upper half of the cloud, Z_{DR} is enhanced
177 while K_{DP} values are low (Fig. 1b-c). Starting at the $-15\text{ }^\circ\text{C}$ isotherm, Z_{DR} sharply decreases and shows an anti-correlation with
178 the enhanced DWR (Fig. 1a) and K_{DP} values. These polarimetric signatures have been reported by previous studies (e.g.,
179 Moisseev et al., 2015 among others), and also the DWR increase below the $-15\text{ }^\circ\text{C}$ level resembles the examples shown in Oue
180 et al. (2018). Oue et al. (2018) concluded in agreement with findings in Moisseev et al. (2015), that an increasing concentration
181 of asymmetric aggregates is partly responsible for enhanced K_{DP} values because the number of small ice particles decrease due
182 to aggregation. The spectrally-resolved Z_{DR} (sZ_{DR} , Fig. 1e), however, reveals that high Z_{DR} -producing, slowly falling ice
183 particles are still present down to the $-5\text{ }^\circ\text{C}$ level. The spectrally resolved DWR (Fig. 1d) shows that the particles falling from
184 above into the DGL are already partly aggregated. At $-17\text{ }^\circ\text{C}$, the spectra are much wider and a new spectral mode appears
185 which is linked to the rapid sZ_{DR} increase (Fig. 1e). The new ice particle mode increases in Doppler velocity and $sDWR$ until
186 20 dB are reached. Unlike Z_{DR} , K_{DP} (Fig. 1c and f) remains at values between 1 and 2 deg km^{-1} down to the $-5\text{ }^\circ\text{C}$ level. A
187 possible explanation of the bimodal spectra - increased sZ_{DR} and K_{DP} - might be secondary ice processes such as collisional
188 fragmentation (Field et al., 2017). The few existing laboratory studies indicate that the number of fragments rapidly increases
189 at $-20\text{ }^\circ\text{C}$, reaching a maximum at $-17\text{ }^\circ\text{C}$ and decreasing again towards $-10\text{ }^\circ\text{C}$ (Takahashi et al., 1995; Takahashi, 2014). This
190 temperature dependence fits well to the observed radar signatures in the DGL, although the laboratory studies only considered
191 collisions of solid ice spheres. As we can exclude strongly rimed particles in the snowfall case shown in Fig. 1, fragile dendritic
192 structures growing on the surface of aggregates might be responsible, which precipitate into the DGL and might easily break

193 into smaller pieces during particle collisions (Fig. 1d). Monte-Carlo Lagrangian super-particle model (Brdar and Seifert, 2018)
194 simulations were recently extended in IMPRINT by a habit prediction scheme and a parameterization of ice collisional
195 fragmentation following Phillips et al. (2017). The role of ice fragmentation and other ice microphysical processes is currently
196 investigated with a radar observation operator for explaining the observed radar signatures of intense aggregation shown in
197 Fig. 1.

198

199 The PROM-project *Investigation of the initiation of convection and the evolution of precipitation using simulations and*
200 *polarimetric radar observations at C- and Ka-band (IcePolCKa)* combines observations of the C-band Polarization Diversity
201 Doppler Radar (POLDIRAD) at the German Aerospace Center (DLR), Oberpfaffenhofen, with those of the Ka-band,
202 Millimeter-wave cloud RADar of the Munich Aerosol Cloud Scanner (miraMACS) at Ludwig-Maximilians-Universität (LMU),
203 Munich. While IMPRINT combines triple-frequency zenith-pointing observations with spectral cloud radar polarimetry,
204 IcePolCKa explores the life cycle of convective precipitation with spatially separated weather and cloud radars in order to
205 quantify ice crystal properties in precipitation formation. The project focuses on ice particle growth and its role in precipitation
206 formation within convective cells. Coordinated Range-Height-Indicator (RHI, varying elevation at constant azimuth) scans
207 along the 23 km long cross-section between both radars allow to observe DWR (Fig. 2a) and Z_{DR} (Fig. 2b) fingerprints of
208 individual convective cells. While the deviation from Rayleigh scattering with increasing ice crystal size at the cloud radar
209 wavelength allows distinguishing regions dominated by aggregation from regions with depositional growth, the slanted
210 perspective of the weather radar helps to narrow down the aspect ratio of ice crystals. Although the DWR technique to infer
211 ice crystal size is well established (e.g. Kneifel et al., 2015), assumptions about the unknown ice crystal shape are necessary.
212 Here, simultaneous polarimetric measurements, like Z_{DR} , help to narrow down estimates of the average asphericity of ice
213 crystals and reduce ambiguities in retrieving ice crystal size and ice water content. IcePolCKa develops an algorithm, which
214 uses Z_H , Z_{DR} and DWR measurements from the two radars to retrieve IWC, the mean particle diameter D_m , and the aspect ratio
215 of ice crystals using a least-squares fit between measurements and T-matrix scattering simulations. The model of horizontally
216 aligned spheroids in combination with an effective medium approximation following Hogan et al (2012) is used to find the
217 simplest ice particle model which explains the multi-wavelength polarimetric measurements. The approach allows studying
218 the covariance of DWR and Z_{DR} while varying particle density, mean particle diameter D_m , and aspect ratio. More sophisticated
219 models, such as discrete dipole approximation (DDA) simulations of specific ice crystals, would require the knowledge of the
220 aspect ratio, and make it hard to identify ice shape collections along these free variables. The multi-wavelength polarimetric
221 measurements are also used as a benchmark for convective precipitation formation in NWP models, where cloud microphysics
222 introduce substantial uncertainty (e.g. Morrison et al., 2020; Xue et al., 2017). In IMPRINT simulated microphysical processes
223 in NWP models will be compared to fingerprints in radar observations: A nested WRF setup covering the overlap area of both
224 radars is used to simulate convective events with microphysical schemes of varying complexity while the Cloud-resolving
225 model Radar SIMulator (CR-SIM; Oue et al., 2020), produces synthetic radar observations, such as DWR (Fig. 2c) and Z_{DR}
226 (Fig. 2d). Fig. 2 illustrates that the Predicted Particle Properties (P3) scheme (Morrison and Milbrandt, 2015) is able to produce

227 DWR features of similar magnitude and variability compared to the observations, while a realistic ice particle asphericity is
228 still missing. IcePolCKa compiled over 30 convective days of polarimetric measurements and simulations with 5 different
229 schemes over a 2-year period, which is currently used to analyse how well these different microphysical schemes reproduce
230 the polarimetric observations. A cell-tracking algorithm (TINT; Fridlind et al., 2019) facilitates the comparison on a cell object
231 basis. Comparison of macrophysical cloud characteristics, such as echo top height or maximum cell reflectivity, show that the
232 model simulates too few weak and small-scale convective cells, independent of the microphysics scheme. In ongoing studies,
233 the P3 scheme seems to better represent radar signatures within the ice phase, while a spectral bin scheme tends to better
234 simulate radar signatures within rain, where all other schemes are not able to correctly reproduce observed Z_{DR} features.

235
236 The PROM-project *A seamless column of the precipitation process from mixed-phase clouds employing data from a*
237 *polarimetric C-band radar, a micro-rain radar and disdrometers (HydroColumn)* characterizes precipitation processes inside
238 a vertical atmospheric column by combining polarimetric Doppler weather radar observations with co-located measurements
239 from micro-rain radars, disdrometers and in-situ measurements, and by relating these observations to the large-scale
240 atmospheric thermodynamics derived from NWP models. To date, spectral analyses are mostly performed with cloud radars
241 operating at shorter wavelengths (see previous paragraphs or, e.g., Shupe et al., 2004; Verlinde et al., 2013; Kalesse et al.,
242 2016; Gehring et al., 2020; Li and Moisseev, 2020), but their implementation across the national C-band radar network offers
243 prospects for operational area-wide applications, e.g. the identification of dominant precipitation particle growth processes
244 such as aggregation or riming. While the operational DWD birdbath scan has so far been used primarily to monitor Z_{DR} (Frech
245 and Hubbert, 2020), *HydroColumn* now also exploits the Doppler spectra measured at C-band for the analysis of
246 microphysical process information. Fig. 3 shows quasi-vertical profiles (QVPs; Trömel et al., 2014; Ryzhkov et al., 2016) of
247 polarimetric variables and Doppler spectra from birdbath scans for a stratiform precipitation event monitored with the
248 Hohenpeißenberg C-band research radar (47.8014N, 11.0097E) of DWD together with in-situ particle images obtained by the
249 Falcon research aircraft from DLR during the BLUESKY campaign (Voigt et al., 2021) within the *POLICE* project
250 (Sect.4.2.1). In-situ measurements have been performed with the Cloud, Aerosol and Precipitation Probe CAPS (Kleine et al.,
251 2018) integrated in a wing station on the Falcon flying within a horizontal distance of about 20 km from the radar site and
252 within about ± 15 min of the radar measurements. The dendritic growth layer (DGL; Ryzhkov and Zrnica, 2019) centered around
253 -15 °C is characterized by Z_{DR} maxima of ~ 1 dB and K_{DP} of ~ 0.2 deg km⁻¹, and a strong Z_H increase towards lower levels
254 (Fig. 3a). Particle images collected at temperatures below about -15 °C indicate mostly small irregular ice particles with the
255 number of larger particles increasing toward -15 °C (see levels L1 and L2 in Fig. 3c), and further down also reveal dendrites
256 and plates (L3, L4). In general, aggregation and riming become highly effective particle growth mechanisms at temperatures
257 around -7 °C (Libbrecht, 2005), and both processes result in a reduction of Z_{DR} (Fig. 3a). The vertically pointing Doppler
258 measurements can be used here to gain a deeper insight into the particle growth process. In this case study, the Doppler
259 measurements illustrated in Fig. 3b indicate typical ice-particle fall speeds increasing to about 2 m s⁻¹ just above the melting
260 layer and thus suggest a transition from predominantly aggregates to moderately rimed particles based on the relationship

261 between Doppler velocity and riming degree found by Kneifel and Moisseev (2020). This conclusion is supported by the
262 corresponding in-situ images showing increasing riming of polycrystals and aggregates toward the melting layer (L6). The
263 analysis confirms the benefit of interpreting radar signatures from polarimetric weather radar observations in combination with
264 vertically pointing Doppler radar measurements, which was previously pointed out for higher-frequency cloud research radars
265 (Oue et al., 2018; Kumjian et al., 2020). This novel application of radar spectral analysis to vertically-pointing operational
266 weather radar scans may provide a more detailed view into intense precipitation events, such as hailstorms, where the use of
267 cloud radars is severely limited due to the strong attenuation at high radar frequencies.

268 **3.2. Anthropogenic modifications of precipitation microphysics**

269 The PROM-project *Polarimetry Influenced by CCN and INP in Cyprus and Chile (PICNICC)* seeks to improve our
270 understanding of aerosol effects on microphysical growth processes in mixed-phase clouds. *PICNICC* exploits unique remote-
271 sensing datasets from the LACROS suite (Radenz et al., 2021) extended with ground-based remote sensing instruments
272 installed at Leipzig University, Universidad de Magallanes (Punta Arenas), and Cyprus University of Technology (Limassol).
273 Thus, dual-frequency polarimetric radar observations from the polluted, aerosol-burden Northern and from the clean, pristine
274 Southern hemisphere can be contrasted for microphysical process studies as already performed in the project for stratiform
275 mixed-phase clouds to investigate inter-hemispheric contrasts in the efficiency of heterogeneous ice formation (Radenz et al.,
276 2021). The PICNICC project challenges the hypothesis that higher ice crystal concentrations favour aggregation, which
277 is expected to be more frequent for high aerosol loads and accordingly higher ice nucleating particle (INP) concentrations,
278 while riming should prevail when supercooled liquid layers are sustained due to a scarcity of INP. Evaluating this hypothesis
279 requires the distinction between aggregation and riming in mixed-phase cloud systems. Fig. 4 demonstrates for a deep mixed-
280 phase cloud system passing the low-aerosol site in Punta Arenas (53°S, 71°W), Chile, on 30 August 2019, the capability of
281 the LACROS suite to distinguish between aggregates and rimed particles when combined with a 94-GHz Doppler radar. The
282 pattern of the 94-GHz radar reflectivity factor (Z , Fig. 4a) underlines the complex structure of the system. The height
283 spectrogram of the vertical-pointing 94-GHz slanted linear depolarization ratio (SLDR, Fig. 4 e) from 08:30 UTC exhibits
284 regions of changing shape signatures and multi-modality in the cloud radar Doppler spectra, where multiple hydrometeor
285 populations coexist. The polarizability ratio ξ_e (Myagkov et al., 2016; Fig. 4d) obtained from the RHI scans of SLDR and the
286 co-cross correlation coefficient of horizontal and vertically polarized channels in the slanted basis ρ , at 35 GHz (Fig. 4 b, c)
287 allows to estimate a density-weighted hydrometeor shape. SLDR is more suited for shape classification compared to LDR. By
288 slanting the polarization basis by 45 deg, the returned LDR signatures are much less sensitive to the canting angle distribution
289 of the targets, especially at low elevation angles (Matrosov et al., 2001; Myagkov et al., 2016). The polarimetric RHI scans
290 and the Doppler spectra data enable the retrieval of the vertical profile of the hydrometeors: Columnar-shaped bullet rosettes
291 are formed between 2.5 km height and cloud top as indicated in the RHI scans by an elevation-constant SLDR (Fig. 4b) and
292 an increase of ρ , with decreasing elevation (Fig. 4c). ξ_e values around 1.3 (Fig. 4d) are characteristic for slightly columnar
293 crystals. The decreasing elevation-dependence of ρ , already at around 3 km height (-15 to -20°C) suggests more random

294 particle orientations; here the W-band SLDR spectra (Fig. 4e) show reduced values, likely due to the co-existence of dendritic
295 ice crystals, which are formed preferably in this temperature range. The co-location of dendrites and columnar crystals can be
296 explained by either splintering of the arms of the dendritic crystals or a mixing of locally produced dendrites with columnar
297 crystals from higher up, or both. Below 2.5 km, ξ_c decreases toward unity, indicating the growth of isometric particles. In
298 addition, the vertical-pointing W-band SLDR slowly decreases toward the cloud base, while fall velocities increase (Fig. 4e).
299 Both features are characteristic for riming, which is corroborated by co-located lidar observations that indicate liquid water in
300 the cloud-base region (not shown). Doppler spectra profiles such as the one presented in Fig. 4e are also used in a new neural-
301 network-based riming detection algorithm recently tailored by Vogl. et al. (2021) for vertical-pointing cloud radar
302 observations. This new approach is insensitive to the mean Doppler velocity, which is - especially at Punta Arenas - strongly
303 influenced by orographic mountain waves, because the radar reflectivity factor, skewness and the edge width of the Doppler
304 spectrum is used instead.

305

306 The PROM-project *Investigating the impact of Land-use and land-cover change on Aerosol-Cloud-precipitation*
307 *interactions using Polarimetric Radar retrievals (ILACPR)* analyzes polarimetric radar observations and model simulations
308 simultaneously in order to improve our understanding of land-aerosol-cloud-precipitation interactions. The Terrestrial Systems
309 Modelling Platform (TSMP; Shrestha et al., 2014; Gasper et al., 2014) developed under the DFG-funded Transregional
310 Research Center TR32 (Simmer et al., 2015) is used to simulate summertime convective storms passing the polarimetric X-
311 band radar (BoXPoL, e.g. Diederich et al., 2015a,b) located in Bonn, Germany. TSMP generally underestimates the convective
312 area fraction, high reflectivities, and the width/magnitude of differential reflectivity (Z_{DR}) columns indicative of updrafts, all
313 leading to an underestimation of the frequency distribution for high precipitation values (Shrestha et al., 2021a). A decadal
314 scale simulation over the region using the hydrological component of TSMP also shows that much of the variability in the
315 simulated seasonal cycle of shallow groundwater could be linked to the distribution of clouds and vegetation (Shrestha, 2021),
316 which further emphasizes the importance of evaluating the representation of clouds and precipitation in numerical models. The
317 fusion of radar observations and models with the aid of observation operators allows for an extended interrogation of the effects
318 of anthropogenic interventions on precipitation generating processes and the capabilities of numerical models to reproduce
319 them. Here, findings from one simulated hailstorm observed on 5 July 2015 passing the city of Bonn, Germany, are explained.
320 Sensitivity simulations are conducted using large-scale aerosol perturbations and different land-cover types reflecting actual,
321 reduced and enhanced human disturbances. While the differences in modelled precipitation in response to the prescribed
322 forcing are below 5 %, the micro- and macrophysical pathways differ, acting as a buffered system to the prescribed forcings
323 (Stevens and Feingold, 2009; Seifert and Beheng, 2012). Fig. 5 shows vertical cross-sections reconstructed from volume scans
324 measured with BoXPoL together with simulated Z_H and Z_{DR} for the TSMP simulations with actual land-cover but perturbed
325 condensation nuclei (CN) and ice nucleating particle (INP) concentrations. CN concentrations are 100 cm^{-3} for maritime and
326 1700 cm^{-3} for continental aerosol. Similarly, default INP concentrations for dust, soot and organics are $162\text{E}3 \text{ m}^3$, $15\text{E}6 \text{ m}^3$
327 and $177\text{E}6 \text{ m}^3$, respectively. For low/high INP, the concentration of soot and organics are decreased/increased by one order of

328 magnitude. To generate the synthetic radar observations the Bonn Polarimetric Radar observation Operator, B-PRO, (Xie et
329 al., 2021; Xie et al., 2016; Heinze et al., 2017; Shrestha et al., 2021b) is applied. B-PRO is based on the non-polarimetric
330 version of EMVORADO (Zeng et al., 2016); its code part for computing unattenuated radar reflectivity on the original model
331 grid (Blahak, 2016) has been expanded to unattenuated polarimetric variables based on spheroidal shape assumptions (T-
332 matrix). Because the full polarimetric version of EMVORADO (Pol-EMVORADO, see Section 4.1) was only released very
333 recently, the model data in ILACPR has been processed using B-PRO. Preliminary comparisons between B-PRO and Pol-
334 EMVORADO (not shown here) exhibit negligible differences in their results on the model grid, but Pol-EMVORADO is much
335 more computationally efficient and takes effects of beam broadening and attenuation along the actual radar ray paths into
336 account. The vertical cross sections are compared at different times marked by the vertical grey bars in the time series of
337 Convective Area Fraction (CAF, Fig. 5 a), defined as the ratio of area with $Z_H > 40$ dBZ (at 2 km a.g.l.) to total storm area. On
338 average BoXPol observations show a bit higher CAF compared to the simulations. The evolution is always similar in terms of
339 an initial increase and intensification in the second part of the observation period, where the experiment with maritime aerosols
340 and low INP (Mar-lowIn) is closest to the observations. All simulations show Z_H and Z_{DR} patterns comparable to BoXPol
341 observations, however, the experiment with continental aerosol and default INP (Con-defIN, Fig. 5c) shows weaker Z_H while
342 Mar-lowIN (Fig. 5d) shows somewhat higher Z_H values compared to BoXPol (see Fig 5a). The simulations with maritime CN
343 produce low cloud droplet concentrations with larger mean diameters compared to the simulations with continental CN.
344 Accompanied by a very strong updraft, this also leads to high concentrations of supercooled raindrops above the melting layer
345 with broader spatial extent (due to a broader updraft region) compared to the simulations with continental CN and contributes
346 to an enhanced growth of hail resulting in higher Z_H . Also, as shown in the CAF time series, simulations with continental
347 aerosol and default/high IN tend to exhibit similar behaviour in radar space, with the latter exhibiting higher CAF only at latter
348 stages of the storm. The continental CN simulations with default and high IN differ in terms of simulated updraft speed and
349 total hydrometeor content, being higher for the latter one. However, Cont-highIN produces smaller graupel and hail particles
350 compared to Cont-defIN, resulting in similar Z_H . The experiment with continental aerosol and high INP concentration (Con-
351 highIN, not shown) generates similar polarimetric moments to Con-lowIN. All experiments exhibit vertically extensive
352 columns of (slightly) enhanced Z_{DR} , collocated with intense simulated updrafts reaching up to 13 to 14 km. Indeed, Z_{DR}
353 columns emerged as proxies for updraft strength and ensuing precipitation enhancement (Weissmann et al., 2014; Simmer et
354 al., 2014; Kumjian et al., 2014; Kuster et al., 2020), and research on their exploitation for nowcasting and data assimilation is
355 ongoing. In Fig. 5c/d synthetic Z_{DR} columns are vertically extensive, while Z_{DR} values within the column stay below 0.3 dB.
356 BoXPol observations show Z_{DR} columns reaching up to 6 km height only but with Z_{DR} values exceeding 1dB. While Z_{DR} values
357 in the lower part of the columns are mostly generated by large raindrops, freezing drops and wet hail determine Z_{DR} in the
358 upper parts of the column (Kumjian et al., 2014; Snyder et al., 2015). The diverging appearance of observed and synthetic Z_{DR}
359 columns may point to deficiencies in the treatment of raindrops undergoing freezing and motivates further research. Too rapid
360 freezing of drops combined with graupel generated from the frozen drops may generate enhanced but still low Z_{DR} up to high
361 altitudes. Following Ilotoviz et al. (2018) such attributes of Z_{DR} columns are highly determined by the vertical velocity, hail

362 size, and aerosol concentration, e.g. higher CN concentrations lead to higher columns with higher Z_{DR} values inside and also
363 higher Z_H . In this case study and the specific time step shown, Mar-lowIN (i.e. with lower CN concentration) shows a wider
364 and somewhat taller Z_{DR} column together with a more intense Z_H core (compare Fig. 5c/d). Further explanations require an
365 improved representation of the Z_{DR} columns in the model.

366 **4 Fusion of radar polarimetry and atmospheric models**

367 Probably the most important and central tool for connecting polarimetric observations with numerical atmospheric models are
368 observation operators, which generate virtual observations from the model state. These virtual observations can be
369 directly compared with the real observations and signatures of microphysical processes including their temporal evolution.
370 Thus, the accuracy of precipitation and cloud parameterizations can be indirectly evaluated and a database established for
371 model optimization. Missing polarimetric process fingerprints (e.g. Kumjian, 2012) in the virtual observations may hint at
372 model deficiencies, and model parameterizations can be adapted in order to increase the coherence between real and virtual
373 observations. Moreover, sufficiently accurate and fast observation operators are mandatory for the direct assimilation of
374 observations using ensemble methods.

375 However, bulk cloud microphysical parameterizations required for NWP models include assumptions on several critical
376 parameters and processes which are not explicitly prognosed or resolved by the governing numerical model. An example are
377 the inherently assumed particle size distributions and their relations to the prognostic moments (hydrometeor mass and number
378 densities). Another challenge is the handling of hydrometeor parameters that are not or only insufficiently constrained by the
379 model's microphysics but are highly relevant for the calculation of virtual observations in the (radar) observation operator. For
380 example, the melting state as well as shape, microstructure, and spatial orientation of the different hydrometeors are not
381 prognostic (or not even implicitly assumed) in most operational bulk schemes. Therefore, suitable assumptions are required in
382 observation operators in order to compute meaningful virtual observations. Moreover, bulk cloud microphysical schemes may
383 only insufficiently approximate the natural variability, and the interactions between the few assumed hydrometeor classes and
384 the size distribution moments are mainly tuned to get, e.g., the surface precipitation right. The current approximations in both
385 numerical models and observation operators may hence translate into different sources of errors and biases of the simulated
386 radar variables (e.g. Schinagl et al., 2019; Shrestha et al., 2021b). As an example, Fig. 7 shows too low polarimetric signals
387 above the melting layer, which are partly caused by assumptions inherent in the observation operator (see Sect. 4.2.1). Such
388 problems challenge both model evaluation and data assimilation. Accordingly, central science questions concern the realism
389 of the sensitivities of simulated radar variables to parameters in the observation operators and the models as well as effective
390 approaches for the evaluation and improvement of moist processes parameterizations.

391 Another challenge for large-scale applications such as long-term model evaluations or operational real-time data assimilation
392 based on large radar networks is the high computational demand and low speed of current polarimetric radar observation
393 operators. Often, the operators apply some kind of pre-calculated lookup tables (LUT) of scattering properties and

394 parallelization techniques for speed optimizations (e.g. Wolfensberger and Berne, 2018; Matsui et al., 2019; Oue et al., 2020).
395 Despite that, radar simulations for a single time step take - depending on the computer - on the order of minutes for one single
396 plan position indicator (PPI) scan (Wolfensberger and Berne, 2018) or for a single model scene (CR-SIM; Oue et al., 2020).
397 Matsui et al. (2019) state the LUT generation process of their POLARRIS operator to only take a few minutes when distributed
398 to few thousands of processors, but do not elaborate on the required times for the actual simulation of the radar measurement.
399 The operator B-PRO (Xie et al., 2016), which uses neither of these techniques, is much slower, as applications within SPP-
400 PROM have demonstrated (Shresta et al., 2021b). While acceptable for research, real-time operational applications may pose
401 much stricter time constraints. Therefore, an important technical goal is to provide an efficient, yet physically accurate and
402 “state-of-the-art”, polarimetric radar operator to the community, which reduces the simulation time for multi-elevation PPI
403 scans of many stations to a few seconds.

404 **4.1 Polarimetric radar observation operator development**

405 Within the PROM-project *Operation Hydrometeors*, the up-to-now non-polarimetric radar observation operator
406 EMVORADO (Zeng et al., 2016; Blahak and de Lozar, 2020; Blahak, 2016) has been extended to polarimetry (Mendrok et
407 al., 2021). (Non-polarimetric) EMVORADO has been designed to efficiently simulate PPI volume scan measurements of entire
408 radar networks from the prognostic model state of an NWP model for direct comparisons with the radar observations.
409 EMVORADO is part of the executable of both the COSMO and ICON NWP models, which allows to run the operator within
410 a NWP model run and to access the model state and radar variables in memory. The code is MPI- and OpenMP-parallelized
411 and thus fully exploits the computational power of modern HPCs and avoids storing and re-reading extensive model state data
412 to/from hard drives. This enables large-scale real-time applications such as operational data assimilation and extensive NWP
413 model verifications using whole radar networks at high temporal resolution. Its modular nature allows for relatively easy
414 interface development to other NWP models. An offline framework is also available, which accesses model states of one model
415 time step from hard disk. EMVORADO includes detailed modular schemes to simulate beam bending, beam broadening and
416 melting effects, and allows users to choose for each process between computationally cheap and physically accurate options.
417 The operator has been used for the assimilation of radar reflectivity with positive impact on precipitation forecasts (Bick et al.,
418 2016; Zeng et al., 2018; 2019; 2020). Currently, DWD uses EMVORADO to operationally assimilate 3D volumetric
419 reflectivity and radial wind observations of its C-band radar network. Key for this application is also the extensive use of
420 precomputed lookup tables that relate (Mie-theory based) bulk reflectivity directly to hydrometeor densities and temperature.
421 The effects of neglecting radar beam pattern and broadening and of hydrometeor fall speeds on data assimilation have been
422 investigated in a joint effort together with the PROM-project *Representing model error and observation Error uncertainty
423 for Data assimilation of POLarimetric radar measurements (REDPOL)* (Zeng et al., 2021a).
424 The polarimetry-extended EMVORADO, in the following referred to as Pol-EMVORADO, has inherited all features of
425 EMVORADO, which in turn have been expanded where necessary to calculate and handle polarimetric variables. This
426 includes, e.g., beam bending, beam broadening, and beam smoothing schemes, effective medium approximations allowing 1-

427 and 2-layered hydrometeors with different water-ice-air mixing schemes and melting topologies, and a lookup table approach
428 for an efficient access to polarimetric observables such as Z_{DR} , LDR , ρ_{HV} , and K_{DP} . Optionally, attenuation effects can be
429 considered, specific and differential attenuation (A_H and A_{DP} , respectively) provided, and further output quantities derivable
430 from the complex scattering amplitudes easily added. Pol-EMVORADO applies state-of-the-art scattering properties of
431 spheroidal particles derived by one-layered (Mishchenko, 2000) and two-layered T-Matrix approaches (Ryzhkov et al., 2011).
432 Assumptions on spheroid shape and orientation follow parameterizations introduced in Ryzhkov et al. (2011). The lookup
433 table approach has been revised to accommodate additional parameters necessary to derive the full set of polarimetric radar
434 output. For a given set of parameters affecting the hydrometeor scattering properties, the lookup tables are created only once,
435 stored in files, and re-used for subsequent runs.

436 Using pre-existing lookup tables, the computations for virtual polarimetric volume scans of radar networks are very fast.
437 Foreexample, simulating the volume scan observations of all polarimetric parameters for all 17 German radars takes a few
438 seconds only on a Linux workstation (8 cores) and adds only about 1 s per radar output time step to the model runtime when
439 performed online during a run of ICON-D2 (DWD's operational convection-allowing ICON version with 2 km grid spacing)
440 on DWD's NEC Aurora supercomputer. That is, simulating polarimetric radar data in intervals of 5 min as observed by DWD's
441 weather radar network adds only a few percent of the total model runtime (Mendrok et al., 2021) enabling the exploitation of
442 Pol-EMVORADO for the assimilation of high temporal resolution polarimetric radar data in an operational framework. Pol-
443 EMVORADO has been incorporated into the official version of EMVORADO and can be run online (i.e. within a COSMO
444 or ICON run) as well as offline (i.e. stand-alone with model fields from data files). Although designed as a PPI volume scan
445 observation operator for a radar network, its output can also be provided on NWP model grids. An example of a Z_{DR} volume
446 scan simulated by Pol-EMVORADO for the **REDPOL** project is shown in Fig. 6 (see also Sect. 4.2.3).

447 In summary, (Pol-)EMVORADO comprises a wide set of state-of-the-art features. While each of these features is provided
448 also by other observation operators, (Pol-)EMVORADO is, to our knowledge, unique in combining them into one operator
449 that allows to simulate virtual observations, including instrumental effects and in formats directly comparable to real
450 observational scans, from NWP model runs in a comparably accurate and very fast manner targeted at operational applications.
451 Mendrok et al. (2021) give a comprehensive description of the features developed or updated for Pol-EMVORADO including
452 details on their implementation and performance.

453 However, from the application of Pol-EMVORADO (or B-PRO, see Sect. 3.2) within PROM, a number of problems became
454 evident. Modeling hydrometeors as homogeneous effective-medium particles (e.g. oblate spheroids) does not reproduce well
455 the polarimetric signatures of low density hydrometeors like dendrites or aggregates typical for snow while keeping their
456 microphysical properties (e.g. aspect ratio, degree of orientation) within realistic - observed or model-predicted - ranges and
457 consistent between different radar frequencies. This deficiency has been demonstrated and explained from electromagnetic
458 theory by Schrom et al. (2018). It is obvious in one case study (Shrestha et al., 2021b) and in Fig. 7, where Z_{DR} and K_{DP} in the
459 snow-dominated layer between 2.5 and 5 km height almost entirely lack the typical observed features, i.e. bands of enhanced
460 Z_{DR} and K_{DP} in the dendritic growth layer that then smoothly decrease to mostly positive, non-zero values towards the melting

461 layer. This deficiency can also be observed with other polarimetric observation operators applying a T-matrix approach (see
462 simulation-to-observation comparisons in Wolfensberger and Berne (2018), Matsui et al. (2019), Oue et al. (2020), where the
463 lack of Z_{DR} and K_{DP} signatures is not discussed at all or exclusively explained by a lack of secondary ice, though), which
464 nevertheless currently constitutes the state-of-the-art in radar polarimetry. Orientation and shape of frozen and melting
465 hydrometeors are very variable, both in nature and in the assumptions used in observation operators, which translates into large
466 uncertainties in polarimetric radar signatures (e.g., Matsui et al., 2019; Shrestha et al., 2021b).

467 To tackle these challenges, it is planned to interface Pol-EMVORADO to scattering databases or other scattering models in
468 order to enable more realistic cloud ice and aggregate snowflake scattering properties and allow for improvements or
469 extensions of the polarimetry-related microphysical assumptions (shape/habit/microstructure, orientation and their
470 distribution, e.g., Wolfensberger et al., 2018), particularly for (partly-)frozen hydrometeors. For PROM's 2nd phase, we have
471 proposed to take this up guided with Lagrangian particle model information as well as to test the application of Pol-
472 EMVORADO in an operational data assimilation environment.

473 **4.2 Model evaluation and improvements using forward simulations and microphysical retrievals**

474 **4.2.1 Convection-resolving simulations with COSMO**

475 In a joint effort, the PROM-projects *Operation Hydrometeors* and *ILACPR* evaluate simulated stratiform precipitation events
476 in radar observation space and develop a sophisticated polarimetry-based hydrometeor classification and quantification for the
477 evaluation of the representation of hydrometeors in numerical models. Based on a stratiform event monitored on 7 October
478 2014 with the Bonn polarimetric X-band radar BoXPoL, Fig. 7 illustrates the potential of using polarimetric observations for
479 the evaluation and improvement of microphysical parameterizations. Fig. 7 a-f compare QVPs of measured and virtual Z_H ,
480 Z_{DR} , and K_{DP} with the Bonn Polarimetric Radar observation Operator B-PRO (Xie et al., 2021) to forecasts simulated with
481 COSMO version 5.1 using its 2-moment cloud microphysics scheme (itype_gscp=2683; Seifert and Beheng, 2016). Due to a
482 small spatial shift of the precipitation event in the simulations, the observations at 50.7305 N, 7.0717 E are compared with
483 simulations at a close-by grid point at 51.1 N, 7.0717 E. As demonstrated in Shrestha et al. (2021b) using a similar stratiform
484 precipitation event, COSMO tends to simulate considerable amounts of melting graupel partly reaching the surface, which
485 results in higher synthetic Z_{DR} than observed (compare Fig. 7c/d) within and below the melting layer (ML). Above the ML,
486 however, synthetic Z_{DR} already approaches 0 dB at around 6 km height, which indicates deficiencies in the ice-snow
487 partitioning in COSMO as well as in the assumed snow morphology (soft spheroids) in the observation operator, both resulting
488 in too low polarimetric signals. While the observed and simulated Z_H is comparable in terms of structure and magnitude -
489 except a more pronounced observed ML - larger differences exist with respect to K_{DP} above the ML (Fig. 7e/f). While
490 observations show bands of enhanced K_{DP} within the dendritic growth layer (DGL) centred around -15°C , the simulated K_{DP}
491 is very weak indicating a lower concentration of crystals and early aggregates compared to observations (e.g. Moisseev et al.,
492 2015). Ice water content (IWC) above the ML retrieved from measured K_{DP} and differential reflectivity in linear scale Z_{dr} , i.e.
493 $IWC(K_{DP}, Z_{dr})$ following Ryzhkov et al. (2018), agrees well with IWC modelled by COSMO in terms of structure, but has

494 lower magnitudes (compare Fig. 7 g/h) in line with the lower simulated K_{DP} . Overall, Fig. 7 supports the hypothesis of a too
495 strong graupel production in the simulations. *Operation Hydrometeors* also developed a robust radar-based hydrometeor
496 classification (HMC) and mixing ratio quantification algorithm following Grazioli et al. (2015) and Besic et al. (2016, 2018)
497 for the evaluation of the representation of hydrometeors in NWP models (standard output is the dominant hydrometeor type
498 only). This HMC is based on clustering and has the advantage that the radar data are separated into clusters based on their
499 polarimetric similarity (no theoretical preliminary calculation is needed), which are then identified as hydrometeor classes.
500 Various clustering methods can be used here (e.g. Lukach et al. (2021)). The new method is relatively insensitive to
501 uncertainties in the scattering properties of ice particles. Its application to the BoXPoI observations does not indicate graupel
502 below the ML (Fig. 8a), while COSMO simulates a pronounced, thick graupel layer (Fig. 8b) including some melting graupel
503 particles reaching the ground around at 1:45 UTC. Applying the HMC to the virtual observations, however, does not reproduce
504 a graupel layer of similar intensity (Fig. 8c), probably caused by a too strong Z_H and temperature influence (compare with Fig.
505 7) relative to the polarimetric variables in the classification scheme which needs further investigation. A persistent challenge
506 in according routines is that clusters are always separated by the 0 °C-level (e.g. Ribaud et al., 2019), i.e. hail or graupel are
507 identified as clusters only below or above the melting layer. For the case study in Shrestha et al. (2021b) the simulated graupel
508 layer was even more pronounced and sensitivity experiments were performed to guide model improvement: increasing the
509 minimum critical particle diameter D_{crit} , which is required for self-collection of ice particles (aggregation) increased/improved
510 the ice-snow partitioning, and a lower temperature threshold for snow and ice riming, T_{rime} , considerably reduced the graupel
511 production.

512 Comparing state-of-the-art polarimetric retrievals of liquid water content (LWC), ice water content (IWC), particle number
513 concentration N_t and mean particle diameter D_m (e.g. Ryzhkov et al., 2018; Ryzhkov and Zrnica, 2019; Bukovčić et al., 2020;
514 Reimann et al., 2021; Trömel et al., 2019) with their simulated counterparts can also be used for evaluating NWP models and
515 for data assimilation (Carlin et al., 2016). Fig. 7g/h, e.g., shows higher $IWC(K_{DP}, Z_{dr})$ than simulated by COSMO for the case
516 study discussed earlier. However, for more solid conclusions about possible model errors, as well as for the use of retrieved
517 quantities for data assimilation, the retrieval uncertainties must be estimated. The analysis of data collected in the ice regions
518 of tropical convective clouds indicates e.g., that $IWC(K_{DP}, Z_{dr})$ yields a root-mean-square error of 0.49 gm^{-3} with the bias
519 within 6% (Nguyen et al., 2017; 2019). Murphy et al. (2020) introduced the columnar vertical profile (CVP) methodology to
520 follow the track of research aircrafts and better co-locate in-situ data to radar microphysical retrievals. Applying the
521 methodology to two mesoscale convective systems, they found the best performance of polarimetric microphysical retrievals
522 in regions of high Z_{DR} and high K_{DP} but recommend a much larger dataset to finally conclude on the accuracy of these retrievals.

523
524 The PROM-project *POLarimetric signatures of ICE microphysical processes and their interpretation using in-situ*
525 *observations and cloud modelling (POLICE)* evaluates radar retrievals and models using in particular in-situ observations of
526 microphysical cloud parameters from the research aircrafts HALO (e.g. Wendisch et al., 2016; Voigt et al., 2017) and Falcon
527 (e.g. Voigt et al., 2010; Voigt et al., 2014; Flamant et al., 2017). Currently, ground-based polarimetric radar measurements and

528 aircraft in-situ data from the Olympic Mountain Experiment OLYMPEX (Houze et al., 2017; Heymsfield et al., 2018) are
529 exploited to investigate riming processes and to evaluate retrievals of ice water content (IWC), particle number concentration
530 N_t , and mean particle diameter D_m (e.g. Ryzhkov et al., 2018; Ryzhkov and Zrnica, 2019; Bukovčić et al., 2020; Carlin et al.
531 2021). The OLYMPEX mission took place on the Olympic Peninsula of Washington State (USA) from November 2015
532 through February 2016. University of North Dakota's (UND) Cessna Citation II equipped with an in-situ cloud payload
533 overpassed the National Science Foundation (NSF) Doppler On Wheels (DOW, mobile polarimetric X-band radar with about
534 60 km range and 74 m radial resolution), placed in the Chehalis Valley at Lake Quinault (47.48 N, 123.86 W, 64 m altitude)
535 performing RHI scans within an azimuthal sector of 22 deg. Measurements and microphysical retrievals of the DOW and the
536 Citation, respectively, are currently evaluated and will then be compared at matched space-time coordinates for several flight
537 transects.

538

539 **4.2.2 Climate simulations with ICON-GCM**

540 A major part of the uncertainties in representing clouds and precipitation in atmospheric models can be attributed to unresolved
541 variability that affects resolved variables via non-linear processes. Current climate model horizontal resolutions are on the order
542 of 100 km. But even for NWP models, which have resolutions between 10 km for global and 1 km for regional simulations,
543 most cloud processes remain unresolved. The project *Climate model Parameterizations informed by Radar (PARA)*
544 evaluates and improves the representation of cloud and precipitation processes in particular for climate models and focuses on
545 precipitation formation in ice clouds. Since most surface precipitation over continents and extra-tropical oceans involve the
546 ice phase (Mülmenstädt et al., 2015; Field and Heymsfield, 2015) its reliable representation is paramount and thus the focus
547 of *PARA*. Microphysical parameterizations typically consider only the mean cloud liquid or ice water content to compute
548 process rates, which causes biases in all nonlinear processes including radiation (e.g., Cahalan, 1994; Carlin et al., 2002) and
549 precipitation formation (e.g., Pincus and Klein, 2000). Realistic results thus require the tuning of process rates (e.g., Rotstayn,
550 2000) or realistic estimates of subgrid-scale cloud variability and its inclusion in the process parameterizations. To tackle this
551 issue, *PARA* exploits inherent model assumptions for treating fractional cloudiness. Since the early works of Sommeria and
552 Deardorff (1977), atmospheric models assume or predict some notion of subgrid-scale variability of relative humidity. Some
553 models do so by predicting cloud fraction (e.g., Tiedtke, 1993), others use a diagnostic representation of the subgrid-scale
554 probability density function (PDF) of total water specific humidity, q_t (e.g., Sundqvist et al., 1989; Smith, 1990; Le Treut and
555 Li, 1991; Rosch et al., 2015). Another option is to utilize a prognostic probability density function (PDF) of q_t by assuming a
556 functional form and predicting the shape parameters of the PDF (e.g., Tompkins, 2002; Neggers, 2009). The German climate
557 and weather prediction model ICON in its version dedicated to climate simulations (general circulation model version; ICON-

558 GCM) inherits the representation of physical processes from its predecessor ECHAM6 (Stevens et al., 2013) and uses the
559 Sundqvist et al. (1989) parameterization for a diagnostic PDF of the total-water specific humidity, q_t .

560 As a first step, *PARA* analyses the implied PDF of cloud ice using satellite observations from combined CloudSat-CALIPSO
561 radar-lidar satellite observations (DARDAR, Delanoë et al., 2014). Interestingly, a first direct comparison of IWC profiles
562 obtained from DARDAR with polarimetric retrievals based on the ground-based BoXPol radar shows an overall good
563 agreement, except for columns with an integrated ice water path $IWP > 1 \text{ kg m}^{-2}$. In these regions pronounced polarimetric
564 signatures result in high IWC at higher altitudes, which are neither reproduced by reflectivity-only retrievals nor by the
565 DARDAR retrievals. The statistics are currently evaluated on a larger database, which is also used to investigate the impact
566 on the parameterizations in ICON-GCM. In the second step, a stochastic parameterization approach is taken to allow for an
567 unbiased computation of cloud microphysical process rates on average. Based on the cumulative distribution function (CDF),
568 a random number generator draws from the CDF according to the simulated likelihood a plausible value of the specific ice
569 mass based on which the microphysical process is computed. This specifically considers the formation of solid precipitation
570 (snow) from ice clouds via aggregation and accretion processes (Lohmann and Roeckner, 1996; Stevens et al., 2013), and
571 subsequently the evaporation of precipitation below the clouds. The result of the revised aggregation parameterization is shown
572 in Fig. 9. The increased aggregation rate, which is a linear function of the specific cloud ice, q_i , leads to an average decrease
573 in q_i . The aggregation rate is directly linked to the accretion rate, which lowers the effect of q_i decrease. An investigation of
574 the influence of the revised aggregation parameterization on the different microphysical process rates - which are related to
575 the ice phase - is currently performed. A detailed evaluation of the new versus old parameterization with the ground-based
576 polarimetric radar is on its way, and will in particular focus on the time scales of evaporation of precipitation below the cloud.

577 **4.2.3 Data assimilation**

578 Within an idealized framework, Jung et al. (2008; 2010) and Zhu et al. (2020) demonstrated benefits of assimilating simulated
579 polarimetric data for the estimation of microphysical state variables. Up to now, however, direct assimilation of real
580 polarimetric data poses great challenges due to the deficiencies of cloud and precipitation schemes in NWP models in
581 realistically representing and providing the necessary information (optimally the distribution of particle size, shape and
582 orientations in all model grid boxes) required by a polarimetric radar observation operator and therefore causing large
583 representation error (Janjic et al., 2018). Both the specification of model error to examine uncertainty in microphysics (Feng
584 et al., 2021) and the specification of the observation error for polarimetric radar observations that include estimates of the
585 representation error (Zeng et al., 2021b), are investigated in the PROM-project *REDPOL*. For the assimilation of radar
586 reflectivity with an ensemble Kalman filter, several approaches for including model errors during data assimilation are
587 explored, including 1) additive noise with samples representing large-scale uncertainty (see Zeng et al., 2018), 2)
588 combination of large scale and unresolved scale uncertainty (Zeng et al., 2019), and finally 3) adding to these warm bubble
589 triggering of convective storms in case they are missing in the one hour forecast but present in corresponding observations

590 (Zeng et al., 2020). Applying Pol-EMVORADO to the analysis obtained by assimilating radar reflectivity from the German
591 C-band network), Fig. 6 illustrates the resulting differences of these three techniques in Z_{DR} -space. Obviously, synthetic Z_{DR}
592 values depend on the strategy used to specify the model error, putting another weight to the argument that assimilation of radar
593 reflectivity alone is not sufficient to constrain the estimation of microphysical state variables, and that polarimetric information
594 is required in addition. First results in this direction were reported by Putnam et al. (2019), who assimilated Z_{DR} below the
595 melting layer but reported problems with the assimilation of K_{DP} data for a supercell case due to high observation errors as a
596 result of contamination from wet hail, dust and debris and nonuniform beam filling.

597 .

598 **5 Summary and Perspectives**

599 The Priority Programme *Polarimetric Radar Observations meet Atmospheric Modelling (PROM)* (SPP 2115,
600 <https://www2.meteo.uni-bonn.de/spp2115/>) was established in April 2017 by the Senate of the Deutsche
601 Forschungsgemeinschaft (DFG, German Research Foundation) and is designed to run for six years. PROM is a coordinated
602 effort to foster partnerships between cloud modelers and radar meteorologists and thus to accelerate the exploitation of
603 polarimetric weather radars to improve the representation of cloud and precipitation processes in numerical models. The first
604 funding phase engaged in an as-complete-as-possible exploitation and understanding of nation-wide polarimetric
605 measurements complemented by state-of-the-art measurement devices and techniques available at supersites. Bulk
606 polarimetric measurements available over Germany are complemented with multi-frequency observations and spectral
607 polarimetry for detailed studies of ice and cloud microphysics. Thus, modellers now hold an unprecedented amount of three-
608 dimensional microphysics-related observational data in their hands to improve parameterizations. Key tools for the fusion of
609 radar polarimetry and atmospheric modelling, e.g. the Monte-Carlo Lagrangian particle model McSnow and the polarimetric
610 observation operator Pol-EMVORADO, have been developed. PROM started with detailed investigations of the representation
611 of cloud and precipitation processes in the COSMO and ICON atmospheric models exploiting polarimetric observation
612 operators. First improvements of the 2-moment cloud- and precipitation microphysics scheme are made and more are expected
613 in phase 2. In addition, intercomparisons of microphysics schemes in radar space have been performed. Phase 1 further
614 developed microphysical retrievals, determined their uncertainties and started their exploitation for model evaluation and
615 radar-informed parameterizations. The developed prerequisites pave the way to finally exploit polarimetry for indirect and
616 direct data assimilation in the upcoming second funding phase.

617 Some tools developed in phase 1, however, still require refinement in phase 2. The T-matrix calculations for
618 electromagnetic scattering by spheroidal particles represent only a crude approximation to frozen and mixed-phase
619 hydrometeors, especially for pristine ice particles and aggregate snowflakes at cloud radar wavelengths. It is not possible to
620 reproduce observed polarimetric signatures of snow with the T-Matrix approach (i.e. homogeneous ice-air spheroids) and

621 realistic microphysics (shape, orientation). Refinements include interfacing to a new discrete dipole approximation (DDA)-
622 based scattering data base for realistic ice and snow particles for all relevant weather radar wavelengths and improvements of
623 the melting scheme of graupel and hail.

624 Based on the progress made, the fusion of radar polarimetry and atmospheric modelling can be approached even more
625 aggressively in phase 2. While objective 1 received most attention in phase 1, more projects will exploit the observational
626 insights and tools developed to finally improve parameterizations and assimilate polarimetric information, i.e. more emphasis
627 will be put on objectives 2 and 4 in phase 2. Direct assimilation of polarimetric variables remains challenging, because NWP
628 models need to realistically represent and provide the necessary information required by a polarimetric radar observation
629 operator; ideally the distribution of particle size, shape and orientation would be required in all model grid boxes. Indirect
630 assimilation of polarimetric information (e.g. microphysical retrievals, and process signatures), however, is less demanding to
631 the model and should be pursued in parallel. Modern Bayesian data assimilation techniques are sensitive to both model- and
632 observation operator biases, so that further work on these issues is of great importance for a successful data assimilation.

633

634 **Data availability**

635 The data presented in this paper are available through the authors upon request. Polarimetric radar data from the operational
636 C-band radar network is also available from the German Weather Service (DWD). Specific campaign data will be published
637 in addition.

638

639 **Author contributions**

640 Silke Trömel had the initial idea and mainly organized and structured the joint publication. Silke Trömel, Johannes Quaas, and
641 Clemens Simmer formed the editorial team consolidating the text. All authors contributed to specific sections of the paper and
642 commented on the paper.

643

644 **Competing interests**

645 Johannes Quaas is editor of ACP. The authors declare to have no additional conflict of interest.

646

647 **Special issue statement**

648 This article is the overview article of the ACP/AMT/GMD inter-journal special issue “Fusion of radar polarimetry and
649 numerical atmospheric modelling towards an improved understanding of cloud and precipitation processes”. It is not associated
650 with a conference.

651

652 **Acknowledgments**

653 We gratefully acknowledge the funding of the German Research Foundation (DFG) to initialize the special priority program
654 on the Fusion of Radar Polarimetry and Atmospheric Modelling (SPP-2115, PROM). The work of contributing authors was
655 carried out in the framework of the projects Operation Hydrometeors (Grants TR 1023/16-1 and BL 945/2-1), IcePolCKa (HA
656 3314/9-1 and ZI 1132/5-1), ILACPR (Grant SH 1326/1-1), IMPRINT (Grant KN 1112/3-1), POLICE (Grants TR 1023/13-1
657 and VO 1504/5-1), PARA (Grants QU 311/21-1 and TR 1023/15-1), HydroColumn (Grant FR 4119/1-1), REDPOL (Grant JA
658 1077/5-1), and PICNICC (Grants KA 4162/2-1 and SE 2464/1-1). ILACPR gratefully acknowledges the computing time
659 (project HBN33) granted by the John von Neumann Institute for Computing (NIC)
660 and provided on the supercomputer JUWELS at Jülich Supercomputing Centre (JSC).

661

662

663 **References**

664 Alfieria, L., Thielen, J., and Pappenberger, J.: Ensemble hydro-meteorological simulation for flash flood early detection in
665 southern Switzerland, *J. Hydrol.*, 424, 143-153, doi:10.1016/j.jhydrol.2011.12.038, 2012.

666 Bauer, P., Thorpe, A., and Brunet, G.: The quiet revolution of numerical weather prediction, *Nature* 525, 47–55,
667 doi:10.1038/nature14956, 2015.

668 Besic, N., Gehring, J., Praz, C., Figueras i Ventura, J., Grazioli, J., Gabella, M., Germann, U., and Berne, A.: Unraveling
669 hydrometeor mixtures in polarimetric radar measurements, *Atmos. Meas. Tech.*, 11, 4847–4866, doi:10.5194/amt-11-4847-
670 2018, 2018.

671 Besic, N., Figueras i Ventura, J., Grazioli, J., Gabella, M., Germann, U., and Berne, A.: Hydrometeor classification through
672 statistical clustering of polarimetric radar measurements: A semisupervised approach. *Atmos. Meas. Tech.*, 9(9), 4425-4445,
673 2016

674

675 Bick, T., Simmer, C., Trömel, S., Wapler, K., Stephan, K., Blahak, U., Zeng, Y., and Potthast, R.: Assimilation of 3D-radar
676 Reflectivities with an Ensemble Kalman Filter on the Convective Scale, *Quart. J. Roy. Meteor. Soc.*, 142, 1490–1504, 2016.

677

678 Blahak, U.: RADAR_MIE_LM and RADAR_MIELIB - Calculation of Radar Reflectivity from Model Output, COSMO
679 Technical Report No. 28, Consortium for Small Scale Modeling (COSMO), available online [http://www.cosmo-
680 model.org/content/model/documentation/techReports/docs/techReport28.pdf](http://www.cosmo-model.org/content/model/documentation/techReports/docs/techReport28.pdf), 2016.

681

682 Blahak, U. and De Lozar, A.: EMVORADO - Efficient Modular VOLUME scan RADAR Operator. A User's Guide, Deutscher
683 Wetterdienst, available online http://www.cosmo-model.org/content/model/documentation/core/emvorado_userguide.pdf,
684 2020.

685

686 Brdar, S. and Seifert, A.: McSnow: A Monte-Carlo Particle Model for Riming and Aggregation of Ice Particles in a
687 Multidimensional Microphysical Phase Space, *J. Adv. Model. Earth Syst.*, 10(1), 187–206, doi:10.1002/2017MS001167, 2018.

688

689

690 Bukovčić, P., Ryzhkov, A., and Zrnić, D.: Polarimetric Relations for Snow Estimation—Radar Verification, *Journal of Applied*
691 *Meteorology and Climatology*, 59(5), 991-1009, doi:10.1175/JAMC-D-19-0140.1, 2020

692

693 Bühl, J., Seifert, P., Wandinger, U., Baars, H., Kanitz, T., Schmidt, J., Myagkov, A., Engelmann, R., Skupin, A., Heese, B.,
694 Klepel, A., Althausen, D., and Ansmann, A.: LACROS: The Leipzig Aerosol and Cloud Remote Observations System, in:
695 *SPIE Remote Sensing*, edited by Comeron, A., Kassianov, E. I., Schäfer, K., Stein, K., and Gonglewski, J. D., p. 889002,
696 Dresden, Germany, doi:10.1117/12.2030911, 2013.

697

698 Bühl, J., Seifert, P., Maygkov, A., and Ansmann, A.: Measuring ice- and liquid-water properties in mixed-phase cloud layers
699 at the Leipzig Cloudnet station, *Atmos. Chem. Phys.*, 16, 10609-10620, doi: 10.5194/acp-16-10609-2016, 2016

700

701 Cahalan, R. F.: Bounded cascade clouds: albedo and effective thickness, *Nonlinear Proc. In Geophysics.*, 1, 156-167, 1994.

702

703 Carlin, B., et al.: High-cloud horizontal inhomogeneity and solar albedo bias, *J. Climate*, 15, 2321 – 2339, 2002.

704

705 Carlin, J. T., Ryzhkov, A. V., Snyder, J. C., and Khain, A.: Hydrometeor Mixing Ratio Retrievals for Storm-Scale Radar Data
706 Assimilation: Utility of Current Relations and Potential Benefits of Polarimetry, *Mon. Weather Rev.* 144(8), 2981-3001,
707 doi:10.1175/MWR-D-15-461 0423.1., 2016.

708

709 Carlin, J. T., Reeves, H. D., and Ryzhkov, A. V.: Polarimetric Observations and Simulations of Sublimating Snow:
710 Implications for Nowcasting. *J. Appl. Meteor. Climatol.*, 60(8), 1035-1054, doi:10.1175/JAMC-D-21-0038.1, 2021.

711

712 Costa-Surós, M., Sourdeval, O., Acquistapace, C., Baars, H., Carbajal Henken, C., Genz, C., Hesemann, J., Jimenez, C., König,
713 M., Kretschmar, J., Madenach, N., Meyer, C. I., Schrödner, R., Seifert, P., Senf, F., Brueck, M., Cioni, G., Engels, J. F., Fieg,
714 K., Gorges, K., Heinze, R., Siligam, P. K., Burkhardt, U., Crewell, S., Hoose, C., Seifert, A., Tegen, I., and Quaas, J.: Detection

715 and attribution of aerosol–cloud interactions in large-domain large-eddy simulations with the ICOSahedral Non-hydrostatic
716 model, *Atmos. Chem. Phys.*, 20, 5657–5678, doi:10.5194/acp-20-5657-2020, 2020.

717

718 Delanoë, J., Heymsfield, A. J., Protat, A., Bansemer, A., and Hogan, R. J.: Normalized particle size distribution for remote
719 sensing application, *J. Geophys. Res. Atmos.*, 119, 4204–4227, doi:10.1002/2013JD020700, 2014.

720

721 Diederich, M., Ryzhkov, A., Simmer, C., Zhang, P., and Trömel, S.: Use of specific attenuation for rainfall measurement at
722 X-band radar wavelengths - Part 1: Radar calibration and partial beam blockage estimation, *J. Hydrometeor.*, 16, 2, 487–502,
723 doi: 10.1175/JHM-D-14-0066.1, 2015a.

724

725 Diederich, M., Ryzhkov, A., Simmer, C., Zhang, P., and Trömel, S.: Use of specific attenuation for rainfall measurement at
726 X-band radar wavelengths - Part 2: Rainfall estimates and comparison with rain gauges, *J. Hydrometeor.*, 16, 2, 503–516, doi:
727 10.1175/JHM-D-14-0067.1, 2015b.

728

729 Dipankar, A., Stevens, B., Heinze, R., Moseley, C., Zängl, G., Giorgetta, M., and Brdar, S.: Large eddy simulations using the
730 general circulation model ICON, *J. Adv. Model. Earth Sy.*, 7, 963–986, doi.org/10.1002/2015MS000431, 2015.

731

732 Feng, Y., T. Janjic, Y. Zeng, A. Seifert, J. Min, 2021, Representing microphysical uncertainty in convective-scale data
733 assimilation using additive noise, *J. Adv. Model. Earth Sy.*, 2021 (submitted).

734

735 Field, P. R. and Heymsfield, A. J.: Importance of snow to global precipitation, *Geophys. Res. Lett.*, 42, 9512–9520,
736 doi:10.1002/2015GL065497, 2015.

737

738 Field, P. R., Lawson, R. P., Brown, P. R. A., Lloyd, G., Westbrook, C., Moisseev, D., Miltenberger, A., Nenes, A., Blyth, A.,
739 Chouarton, T., Connolly, P., Buehl, J., Crosier, J., Cui, Z., Dearden, C., DeMott, P., Flossmann, A., Heymsfield, A., Huang,
740 Y., Kalesse, H., Kanji, Z. A., Korolev, A., Kirchgaessner, A., Lasher-Trapp, S., Leisner, T., McFarquhar, G., Phillips, V.,
741 Stith, J., and Sullivan, S.: Secondary Ice Production: Current State of the Science and Recommendations for the Future,
742 *Meteorological Monographs*, 58, 7.1–7.20, doi: 10.1175/AMSMONOGRAPHS-D-16-0014.1, 2017

743 Forster, P., Storelvmo, T., Armour, K., Collins, W., Dufresne, J. L., Frame, D., Lunt, D. J., Mauritsen, T., Palmer, M. D.,
744 Watanabe, M., Wild, M., and Zhang, H.: The Earth’s Energy Budget, Climate Feedbacks, and Climate Sensitivity. In: *Climate*
745 *Change 2021: The Physical Science Basis. Contribution of Working Group I to the Sixth Assessment Report of the*
746 *Intergovernmental Panel on Climate Change*, Cambridge University Press, in press, 2021.

747

748 Frech, M., and Hubbert, J.: Monitoring the differential reflectivity and receiver calibration of the German polarimetric weather
749 radar network, *Atmos. Meas. Tech.*, 13, 1051–1069, doi: 10.5194/amt-13-1051-2020, 2020.

750

751 Gao, W., Sui, C.-H., Chen Wang, T.-C. and Chang, W.-Y.: An evaluation and improvement of microphysical parameterization
752 from a two-moment cloud microphysics scheme and the Southwest Monsoon Experiment (SoWMEX)/Terrain-influenced
753 Monsoon Rainfall Experiment (TiMREX) observations, *J. Geophys. Res. Atmos.*, 116, 1-13, doi:10.1029/2011JD015718,
754 2011.

755

756 Gasper, F., Görden, K., Shrestha, P., Sulis, M., Rihani, J., Geimer, M., and Kollet, S.: Implementation and scaling of the fully
757 coupled Terrestrial Systems Modeling Platform (TerrSysMP v1. 0) in a massively parallel supercomputing environment—a
758 case study on JUQUEEN (IBM Blue Gene/Q), *Geosci. Model Dev.*, 7(5), 2531-2543, 2014.

759

760 Gehring, J., Oertel, A., Vignon, E., Jullien, N., Besic, N., and Berne, A.: Microphysics and dynamics of snowfall associated
761 with a warm conveyor belt over Korea, *Atmos. Chem. Phys.*, 20, 7373–7392, doi: 10.5194/acp-20-7373-2020, 2020.

762

763 Grazioli, J., Tuia, D., and Berne, A.: Hydrometeor classification from polarimetric radar measurements: a clustering approach,
764 *Atmos. Meas. Tech.*, 8(1), 149-170, 2015.

765

766 Flamant, C., Knippertz, P., Fink, A.H., Akpo, A., Brooks, B., Chiu, C.J., Coe, H., Danuor, S., Evans, M., Jegede, O., Kalthoff,
767 N., Konaré, A., Lioussé, C., Lohou, F., Mari, C., Schlager, H., Schwarzenboeck, A., Adler, B., Amekudzi, L., Aryee, J.,
768 Ayoola, M., Batenburg, A.M., Bessardon, G., Borrmann, S., Brito, J., Bower, K., Burnet, F., Catoire, V., Colomb, A., Denjean,
769 C., Fosu-Amankwah, K., Hill, P.G., Lee, J., Lothon, M., Maranan, M., Marsham, J., Meynadier, R., Ngamini, J., Rosenberg,
770 P., Sauer, D., Smith, V., Stratmann, G., Taylor, J.W., Voigt, C., and Yoboué, V.: The Dynamics–Aerosol–Chemistry–Cloud
771 Interactions in West Africa Field Campaign: Overview and Research Highlights, *B. Am. Meteorol. Soc.*, 99, 83–
772 104,doi:10.1175/BAMS-D-16-0256.1, 2018

773

774 Fridlind, A. M., van Lier-Walqui, M., Collis, S., Giangrande, S. E., Jackson, R. C., Li, X., Matsui, T., Orville, R., Picel, M.
775 H., Rosenfeld, D., Ryzhkov, A., Weitz, R., and Zhang, P.: Use of polarimetric radar measurements to constrain simulated
776 convective cell evolution: a pilot study with Lagrangian tracking, *Atmos. Meas. Tech.*, 12, 2979–3000, doi:10.5194/amt-12-
777 2979-2019, 2019.

778

779 Hashino, T., and Tripoli, G. J.: The Spectral Ice Habit Prediction System (SHIPS). Part I: Model Description and Simulation
780 of the Vapor Deposition Process, *J. Atmos. Sci.*, 64(7), 2210-2237, doi:10.1175/JAS3963.1, 2007.

781

782 Heinze, R., Dipankar, A., Henken, C. C., Moseley, C., Sourdeval, O., Trömel, S., Xie, X., Adamidis, P., Ament, F., Baars, H.
783 Barthlott, C., Behrendt, A., Blahak, U., Bley, S., Brdar, S., Brueck, M., Crewell, S., Deneke, H., Girolamo, P. D., Evaristo,
784 R., Fischer, J., Frank, C., Friederichs, P., Göcke, T., Gorges, K., Hande, L., Hanke, M., Hansen, A., Hege, H.-C., Hoose, C.,
785 Jahns, T., Kalthoff, N., Klocke, D., Kneifel, S., Knippertz, P., Kuhn, A., Laar, T., Macke, A., Maurer, V., Mayer, B., Meyer,
786 C. I., Muppa, S. K., Neggers, R. A. J., Orlandi, E., Pantillon, F., Pospichal, B., Röber, N., Scheck, L., Seifert, A., Seifert, P.,
787 Senf, F., Siligam, P., Simmer, C., Steinke, S., Stevens, B., Wapler, K., Weniger, M., Wulfmeyer, V., Zängl, G., Zhang, D.,
788 and Quaas, J.: Large-eddy simulations over Germany using ICON: A comprehensive evaluation, *Q. J. Roy. Meteor. Soc.*, 143,
789 69-100, doi:10.1002/qj.2947, 2017.

790

791 Heymsfield, A., Bansemmer, A., Wood, N. B., Liu, G., Tanelli, S., Sy, O. O., Poellot, M., and Liu, C.: Toward Improving Ice
792 Water Content and Snow-Rate Retrievals from Radars. Part II: Results from Three Wavelength Radar–Collocated In Situ
793 Measurements and CloudSat–GPM–TRMM Radar Data, *J. Appl. Meteor. Climatol.*, 57(2), 365-389. Retrieved Apr 6, 2021,
794 from <https://journals.ametsoc.org/view/journals/apme/57/2/jamc-d-17-0164.1.xml>, 2018.

795

796 [Hogan, R. J., Tian, L., Brown, P. R. A., Westbrook, C. D., Heymsfield, A. J., and Eastment, J. D.: Radar Scattering from Ice](#)
797 [Aggregates Using the Horizontally Aligned Oblate Spheroid Approximation, *J. Appl. Meteor. Climatol.*, 51\(3\), 655-671,](#)
798 [doi:10.1175/JAMC-D-11-074.1, 2012.](#)

799

800 Ilotoviz, E., Khain, A., Ryzhkov, A. V., and Snyder, J. C.: Relation between Aerosols, Hail Microphysics, and ZDR Columns,
801 *J. Atmos. Sci.*, 75, 1755-1781, doi:10.1175/JAS-D-17-0127.1, 2018.

802

803 Janjic, T., Bormann, N., Bocquet, M., Carton, J. A., Cohn, S. E., Dance, S. L., Losa, S. N., Nichols, N. K., Potthast, R., Waller,
804 J. A., and Weston, P.: On the representation error in data assimilation, *Q. J. R. Meteorol. Soc.*, 144:713, 1257-1278, 2018.

805

806 Jung, Y., Xue, M., Zhang, G., and Straka, J.: Assimilation of simulated polarimetric radar data for a convective storm using
807 ensemble Kalman filter. Part II: Impact of polarimetric data on storm analysis, *Mon. Wea. Rev.*, 136, 2246–2260,
808 [doi:10.1175/2007MWR2288.1](#), 2008.

809

810 Jung, Y., Xue, M., and Zhang, G.: Simultaneous Estimation of Microphysical Parameters and the Atmospheric State Using
811 Simulated Polarimetric Radar Data and an Ensemble Kalman Filter in the Presence of an Observation Operator Error, *Mon.*
812 *Wea. Rev.*, 138, 539–562, [doi:10.1175/2009MWR2748.1](#), 2010.

813

814 Jung, Y., Xue, M., and Tong, M.: Ensemble Kalman Filter Analyses of the 29—30 May 2004 Oklahoma Tornadoic
815 Thunderstorm Using One- and Two-Moment Bulk Microphysics Schemes, with Verification against Polarimetric Radar Data,
816 *Mon. Wea. Rev.*, 140, 1457-1475, doi: MWR-D-11-00032.1, 2012

817

818 Kalesse, H., Szyrmer, W., Kneifel, S., Kollias, P., and Luke, E.: Fingerprints of a riming event on cloud radar Doppler spectra:
819 observations and modeling, *Atmos. Chem. Phys.*, 16, 2997–3012, doi: 10.5194/acp-16-2997-2016, 2016.

820

821 Khain, A., Rosenfeld, D., and Pokrovsky, A.: Aerosol impact on the dynamics and microphysics of convective clouds, *Q. J.*
822 *R. Meteorol. Soc.*, 131, 2639–2663, doi:10.1256/qj.04.62, 2005.

823

824 Khain, A. P., Beheng, K. D., Heymsfield, A., Korolev, A., Krichak, S. O., Levin, Z., Pinsky, M., Phillips, V., Prabhakaran, T.,
825 Teller, A., et al.: Representation of microphysical processes in cloud-resolving models: Spectral (bin) microphysics versus
826 bulk parameterization, *Rev. Geophys.*, 53, 247– 322, doi:10.1002/2014RG000468, 2015.

827

828 Kleine, J., Voigt, C., Sauer, D., Schlager, H., Scheibe, M., Kaufmann, S. , Jurkat-Witschas, T., Kärcher, B., and Anderson B.:
829 In situ observations of ice particle losses in a young persistent contrail, *Geophys. Res. Lett.*, doi:10.1029/2018GL079390, 2018.

830

831 Kneifel S., A. von Lerber, J. Tiira, D. Moisseev, P. Kollias, and J. Leinonen: Observed Relations between Snowfall
832 Microphysics and Triple-frequency Radar Measurements, *J. Geophys. Res.*, 120, 6034-6055, doi: 10.1002/2015JD023156,
833 2015.

834

835 Kneifel, S., and Moisseev, D.: Long-term statistics of riming in non-convective clouds derived from ground-based Doppler
836 cloud radar observations, *J. Atmos. Sci.*, 77, 3495–3508, doi: 10.1175/JAS-D-20-0007.1, 2020.

837

838 Kollias, P., Albrecht, B.A., and Marks Jr F.: Why Mie? Accurate observations of vertical air velocities and raindrops using a
839 cloud radar. *Bulletin of the American Meteorological Society*, 83(10), 1471-1484, doi: 10.1175/BAMS-83-10-1471 2002

840

841 Kumjian, M.R.: Principles and applications of dual-polarization weather radar. Part I: Description of the polarimetric radar
842 variables. *J. Operational Meteor.*, 1(19), 226-242, doi: 10.15191/nwajom.2013.0119, 2013

843

844 Kumjian, M. R.: The impact of precipitation physical processes on the polarimetric radar variables, Dissertation, University
845 of Oklahoma, Norman Campus, <https://hdl.handle.net/11244/319188>, 2012

846

847 Kumjian, M. R., Khain, A. P., Benmoshe, N., Ilotoviz, E., Ryzhkov, A. V., and Phillips, V. T. J.: The anatomy and physics of
848 Z_{DR} columns: Investigating a polarimetric radar signature with a spectral bin microphysical model, *J. Appl. Meteor. Climatol.*,
849 53, 1820-1843, 2014.

850

851 Kumjian, M. R., Tobin, D. M., Oue, M., and Kollias, P.: Microphysical insights into ice pellet formation revealed by fully
852 polarimetric Ka-band Doppler radar, *J. Appl. Meteor. Climatol.*, 59, 1557–1580, doi: 10.1175/JAMC-D-20-0054.1, 2020.

853

854 Kuster, C. M., Schuur, T. J., Lindley, T. T., and Snyder, J. C.: Using ZDR Columns in Forecaster Conceptual Models and
855 Warning Decision-Making, *Weather and Forecasting*, 35(6), 2507-2522, 2020.

856

857 Le Treut, H. and Li, Z.-X.: Sensitivity of an atmospheric general circulation model to prescribed SST changes: Feedback
858 effects associated with the simulation of cloud optical properties, *Clim. Dyn.*, 5, 175–187, 1991.

859

860 Li, H., and Moisseev, D.: Two layers of melting ice particles within a single radar bright band: interpretation and implications,
861 *Geophys. Res. Lett.*, 47, e2020GL087499, doi: 10.1029/2020GL087499, 2020.

862

863 Libbrecht, K. G.: The physics of snow crystals, *Rep. Prog. Phys.*, 68, 855–895, doi:10.1088/0034-4885/68/4/R03, 2005.

864

865 Lohmann U. und E. Roeckner, Design and performance of a new cloud microphysics scheme developed for the ECHAM
866 general circulation model, *Clim. Dyn.*, 12, 557-572, 1996.

867

868 Lukach, M., Dufton, D., Crosier, J., Hampton, J.M., Bennett, L. and Neely III, R.R.. Hydrometeor classification of quasi-
869 vertical profiles of polarimetric radar measurements using a top-down iterative hierarchical clustering method. *Atmos. Meas.*
870 *Tech*, 14(2), pp.1075-1098, 2021

871

872 Luke E.P., Yang, F., Kollias, P., Vogelmann, A.M., Maahn, M.: New insights into ice multiplication using remote-sensing
873 observations of slightly supercooled mixed-phase clouds in the Arctic. *PNAS*, 118(13), e2021387118,
874 doi:10.1073/pnas.2021387118, 2021

875 Matrosov, S. Y., Reinking, R. F., Kropfli, R. A., Martner, B. E., and Bartram, B. W. (2001), On the use of radar depolarization
876 ratios for estimating shapes of ice hydrometeors in winter clouds, *Journal of Applied Meteorology*, 40, 479-490,
877 doi:10.1175/1520-0450(2001)040h0479:OTUORDi2.0.CO;2.

878

879 Matsui, T., Dolan, B., Rutledge, S. A., Tao, W.-K., Iguchi, T., Barnum, J., and Lang, S. E.: POLARRIS: A POLARimetric
880 Radar Retrieval and Instrument Simulator, *J. Geophys. Res.-Atmos.*, 124, 4634–4657, doi:10.1029/2018JD028317, 2019.
881

882 Mellado, J.P., Stevens, B., Schmidt, H., and Peters, N.: Buoyancy reversal in cloud-top mixing layers, *Q.J.R. Meteorol. Soc.*,
883 135: 963-978., doi:10.1002/qj.417, 2009.
884

885 Mendrok, J., Blahak, U., Snyder, J. C., and Carlin, J. T.: The polarimetric efficient modular volume scan radar forward operator
886 Pol-EMVORADO, *Geosci. Model Dev.*, 2021 (in preparation for this Special Issue).
887

888 Mishchenko, M. I.: Calculation of the amplitude matrix for a nonspherical particle in a fixed orientation, *Appl. Opt.* 39, 1026-
889 1031, 2000.
890

891 Moisseev, D. N., Lautaportti, S., Tyynela, J., and Lim, S.: Dualpolarization radar signatures in snowstorms: Role of snowflake
892 aggregation, *J. Geophys. Res. Atmos.*, 120, 12 644–12 655, doi:10.1002/2015JD023884, 2015.
893

894 Morrison, H. and Milbrandt, J. A.: Parameterization of Cloud Microphysics Based on the Prediction of Bulk Ice Particle
895 Properties. Part I: Scheme Description and Idealized Tests, *J. Atmos. Sci.*, 72(1), 287-311, 2015.
896

897 Morrison, H., van Lier-Walqui, M., Fridlind, A. M., Grabowski, W. W., Harrington, J. Y., and Hoose, C., et al.: Confronting
898 the challenge of modeling cloud and precipitation microphysics. *Journal of Advances in Modeling Earth Systems*, 12,
899 e2019MS001689. doi:10.1029/2019MS001689, 2020.
900

901 Mülmenstädt, J., Sourdeval, O., Delanoë, J., and Quaas, J.: Frequency of occurrence of rain from liquid-, mixed- and ice-phase
902 clouds derived from A-Train satellite retrievals, *Geophys. Res. Lett.*, 42, 6502-6509, doi:10.1002/2015GL064604, 2015.

903 Murphy, A. M., Ryzhkov, A., & Zhang, P.: Columnar vertical profile (CVP) methodology for validating polarimetric radar
904 retrievals in ice using in situ aircraft measurements. *J. Atmos. Oceanic Technol.*, 37(9), 1623-1642, doi:10.1175/JTECH-D-
905 20-0011.1, 2020.
906

907 Myagkov, A., Seifert, P., Bauer-Pfundstein, M., and Wandinger, U.: Cloud radar with hybrid mode towards estimation of
908 shape and orientation of ice crystals, *Atmos. Meas. Tech.*, 9, 469–489, doi:10.5194/amt-9-469-2016, 2016.
909

910 Neggers, R. A.: A dual mass flux framework for boundary layer convection. Part II: Clouds, *J. Atmos. Sci.*, 66, 1489–1506,
911 doi:10.1175/2008JAS2636.1, 2009.

912

913 Neto, J. D., Kneifel, S., Ori, D., Trömel, S., Handwerker, J., Bohn, B., Hermes, N., Mühlbauer, K., Lenefer, M., and Simmer,
914 C.: The TRIPLE-frequency and Polarimetric radar Experiment for improving process observation of winter precipitation. *Earth*
915 *Syst. Sci. Data*, 11, 845–863, [doi: 10.5194/essd-11-845-2019](https://doi.org/10.5194/essd-11-845-2019), 2019.

916

917 Nguyen, C., Wolde, M., Baibakov, K., and Korolev, A.: Detection and estimation of high ice water content using X- and W-
918 band dual-polarization airborne radar data, 38th Conf. on Radar Meteorology, Chicago, IL, Amer. Meteor. Soc., 89,
919 <https://ams.confex.com/ams/38RADAR/webprogram/Paper321101.html>, 2017.

920

921 Nguyen, C. M., Wolde, M., and Korolev, A.: Determination of ice water content (IWC) in tropical convective clouds from X-
922 band dual-polarization airborne radar, *Atmos. Meas. Tech.*, 12, 5897–5911, [doi: 10.5194/amt-12-5897-2019](https://doi.org/10.5194/amt-12-5897-2019), 2019.

923

924 Ori, D., V. Schemann, M. Karrer, J. Dias Neto, L. von Terzi, A. Seifert, and S. Kneifel: Evaluation of ice particle growth in
925 ICON using statistics of multi-frequency Doppler cloud radar observations, *Q. J. Roy. Meteor. Soc.*, 146: 3830– 3849.
926 [doi:10.1002/qj.3875](https://doi.org/10.1002/qj.3875), 2020

927 Oue, M., A. Tatarevic, P. Kollias, D. Wang, K. Yu, and A.M. Vogelmann: The Cloud-resolving model Radar SIMulator (CR-
928 SIM) Version 3.3: description and applications of a virtual observatory, *Geoscientific Model Development*, 13: 1975-1998.
929 [doi: 10.5194/gmd-13-1975-2020](https://doi.org/10.5194/gmd-13-1975-2020), 2020.

930 Oue, M., Kollias, P., Ryzhkov, A., and Luke, E. P.: Toward exploring the synergy between cloud radar polarimetry and Doppler
931 spectral analysis in deep cold precipitating systems in the Arctic, *J. Geophys. Res. Atmos.*, 123, 2797–2815, [doi: 10.1002/2017JD027717](https://doi.org/10.1002/2017JD027717), 2018.

933 Phillips, V. T. J., Yano, J., & Khain, A. (2017). Ice Multiplication by Breakup in Ice–Ice Collisions. Part I: Theoretical
934 Formulation, *J. Atmos. Sci.*, 74(6), 1705-1719

935 Pfitzenmayer L., Unal, C. M. H., Dufournet, Y., Ruschenberg, H. W. J.: Observing ice particle growth along fall streaks in
936 mixed-phase clouds using spectral polarimetric radar data, *Atmos. Chem. Phys.*, 18, 7843-7863, [doi: 10.5194/acp-18-7843-](https://doi.org/10.5194/acp-18-7843-2018)
937 2018, 2018.

938 Pincus, R. and Klein, S.: Unresolved spatial variability and microphysical process rates in large-scale models, *J. Geophys.*
939 *Res.*, 105, 27059 - 27065, 2000.

940

941 Putnam, B., Xue, M., Jung, Y., Snook, N., and Zhang, G.: Ensemble Kalman Filter Assimilation of Polarimetric Radar
942 Observations for the 20 May 2013 Oklahoma Tornadoic Supercell Case, *Mon. Wea. Rev.*, 147, 2511–2533, [doi:10.1175/MWR-](https://doi.org/10.1175/MWR-D-18-0251.1)
943 [D-18-0251.1](https://doi.org/10.1175/MWR-D-18-0251.1), 2019.

944

945 Radenz, M., Bühl, J., Seifert, P., Baars, H., Engelmann, R., Barja González, B., Mamouri, R.-E., Zamorano, F., and Ansmann,
946 A.: Hemispheric contrasts in ice formation in stratiform mixed-phase clouds: Disentangling the role of aerosol and dynamics
947 with ground-based remote sensing, *Atmos. Chem. Phys. Discuss.* [preprint], <https://doi.org/10.5194/acp-2021-360>, in review,
948 2021.

949

950 Reimann, L., Simmer, C., and Trömel, S.: Dual-polarimetric radar estimators of liquid water content over Germany, Accepted
951 for *Meteorol. Z. (Contrib. Atm. Sci.)*, doi:[10.1127/metz/2021/1072](https://doi.org/10.1127/metz/2021/1072), 2021.

952

953 Ribaud, J.-F., L. A. T. Machado, and T. Biscaro: X-band dual-polarization radar-based hydrometeor classification for Brazilian
954 tropical precipitation systems, *Atmos. Meas. Tech.*, 12, 811–837, doi.org/10.5194/amt-12-811-2019, 2019.

955

956 Rosch, J., et al.: Analysis of diagnostic climate model cloud parameterisations using large-eddy simulations, *Q. J. R. Meteorol.*
957 *Soc.*, 141, 2199-2205, doi:[10.1002/qj.2515](https://doi.org/10.1002/qj.2515), 2015.

958

959 Rotstajn, L. D.: On the tuning of autoconversion parameterizations in climate models, *J. Geophys. Res.*, 105, 15,495–15,507,
960 2000.

961

962 Ryzhkov, A. V., Zrníc, D. S., and Gordon, B. A.: Polarimetric Method for Ice Water Content Determination, *J. Appl. Meteor.*
963 *Climatol.*, 37, 125-134, 1998.

964

965 Ryzhkov, A., Pinsky, M., Pokrovsky, A., and Khain, A.: Polarimetric Radar Observation Operator for a Cloud Model with
966 Spectral Microphysics, *J. Appl. Meteor. Climatol.*, 50, 873-894, 2011.

967

968 Ryzhkov, A., Zhang, P., Reeves, H., Kumjian, M., Tschallener, T., Trömel, S., and Simmer, C.: Quasi-vertical profiles – a
969 new way to look at polarimetric radar data, *J. Atmos. Oceanic Technol.*, 33, 551-562, [doi: 10.1175/JTECH-D-15-0020.1](https://doi.org/10.1175/JTECH-D-15-0020.1), 2016.

970

971 Ryzhkov, A., Bukovcic, P., Murphy, A., Zhang, P., and McFarquhar, G.: Ice Microphysical Retrievals Using Polarimetric
972 Radar Data. In *Proceedings of the 10th European Conference on Radar in Meteorology and Hydrology*, Ede, The Netherlands,
973 1–6 July 2018.

974

975 Ryzhkov, A. and Zrnica, D.: Radar Polarimetry for Weather Observations, Springer Atmospheric Sciences, 486 pp., 2019.
976

977 Schinagl, K., Friederichs, P., Trömel, S., and Simmer, C.: Gamma Drop Size Distribution Assumptions in Bulk Model
978 Parameterizations and Radar Polarimetry and Their Impact on Polarimetric Radar Moments, *J. Appl. Meteor. Climatol.*, 58,
979 467–478, [doi: 10.1175/JAMC-D-18-0178.1](https://doi.org/10.1175/JAMC-D-18-0178.1), 2019.
980

981 Schrom, R. S. and Kumjian, M. R.: Bulk-Density Representations of Branched Planar Ice Crystals: Errors in the Polarimetric
982 Radar Variables, *J. Appl. Meteor. Climatol.*, 57(2), 333-346, 2018.
983

984 Seifert, A. and Beheng, K. D.: A two-moment cloud microphysics parameterization for mixed-phase clouds. Part 1: Model
985 description, *Meteorol. Atmos. Phys.*, 92, 45-66, [doi: 10.1007/s00703-005-0112-4](https://doi.org/10.1007/s00703-005-0112-4), 2006.

986 Shrestha, P., Sulis, M., Masbou, M., Kollet, S. and Simmer, C.: A scale-consistent Terrestrial System Modeling Platform based
987 on COSMO, CLM and ParFlow, *Mon. Wea. Rev.*, 142, 3466-3483, [doi: 10.1175/MWR-D-14-00029.1](https://doi.org/10.1175/MWR-D-14-00029.1), 2014

988 Shrestha, P.: Clouds and vegetation modulate shallow groundwater table depth, 22, 753 – 763, [doi:10.1175/JHM-D-20-0171.1](https://doi.org/10.1175/JHM-D-20-0171.1),
989 2021

990 Shrestha, P., Trömel, S., Evaristo, R., and Simmer, C.: Evaluation of modeled summertime convective storms using
991 polarimetric radar observations, *Atmos. Chem. Phys. Discuss.* [preprint], <https://doi.org/10.5194/acp-2021-404>, in review,
992 2021a.

993 Shrestha, P., Mendrok, J., Pejčic, V., Trömel, S., and Blahak, U.: The impact of uncertainties in model microphysics, retrievals
994 and forward operators on model evaluations in polarimetric radar space, *Geosci. Model Dev.*, 2021b (submitted).
995

996 Shupe, M. D., Kollias, P., Matrosov, S. Y., and Schneider, T. L.: Deriving mixed-phase cloud properties from Doppler radar
997 spectra, *J. Atmos. Oceanic Technol.*, 21, 660–670, [doi: 10.1175/1520-0426\(2004\)021<0660:DMCPFD>2.0.CO;2](https://doi.org/10.1175/1520-0426(2004)021<0660:DMCPFD>2.0.CO;2), 2004.
998

999 Simmel, M., Bühl, J., Ansmann, A., and Tegen, I.: Ice phase in altocumulus clouds over Leipzig: remote sensing observations
1000 and detailed modeling, *Atmos. Chem. Phys.*, 15, 10453–10470, [doi:10.5194/acp-15-10453-2015](https://doi.org/10.5194/acp-15-10453-2015), 2015.
1001

1002 Simmer, C., Thiele-Eich, I., Masbou, M., Amelung, W., Crewell, S., Diekkruöger, B., Ewert, F., Hendricks Franssen, H.-J.,
1003 Huisman, A. J., Kemna, A., Klitzsch, N., Kollet, S., Langensiepen, M., Löhnert, U., Rahman, M., Rascher, U., Schneider, K.,
1004 Schween, J., Shao, Y., Shrestha, P., Stiebler, M., Sulis, M., Vanderborght, J., Vereecken, H., van der Kruk, J., Zerenner, T.,
1005 and Waldhoff, G.: Monitoring and Modeling the Terrestrial System from Pores to Catchments - the Transregional

1006 Collaborative Research Center on Patterns in the Soil-Vegetation-Atmosphere System, B. Am. Meteorol. Soc., 96, 1765–1787,
1007 doi: 10.1175/BAMS-D-13-00134.1, 2015.

1008

1009 Simmer, C., Adrian, G., Jones, S., Wirth, V., Goeber, M., Hohenegger, C., Janjic, T., Keller, J., Ohlwein, C., Seifert, A.,
1010 Trömel, S., Ulbrich, T., Wapler, K., Weissmann, M., Keller, J., Masbou, M., Meilinger, S., Riss, N., Schomburg, A., Vormann,
1011 A., and Weingaertner, C.: HErZ - The German Hans-Ertel Centre for Weather Research. B. Am. Meteorol. Soc., 1057-1068,
1012 doi: [10.1175/BAMS-D-13-00227.1](https://doi.org/10.1175/BAMS-D-13-00227.1), 2014

1013

1014 Smith, R. N.: A scheme for predicting layer clouds and their water content in a general circulation model, Q. J. R. Meteorol.
1015 Soc., 116, 435–460, doi:10.1002/qj.49711649210, 1990.

1016

1017 Snyder, J.C., Ryzhkov, A.V., Kumjian, M.R., Khain, A.P., and Picca, J.C.: A ZDR column detection algorithm to examine
1018 convective storm updrafts, Weather and Forecasting, 30, 1819-1844, 2015.

1019

1020 Sommeria, G. and Deardorff, J. W.: Subgrid-scale condensation models of non-precipitating clouds, J. Atmos. Sci., 34, 344-
1021 355, 1977.

1022

1023 Sourdeval, O., Gryspeerd, E., Krämer, M., Goren, T., Delanoë, J., Afchine, A., Hemmer, F., and Quaas, J.: Ice crystal number
1024 concentration estimates from lidar–radar satellite remote sensing – Part 1: Method and evaluation, Atmos. Chem. Phys., 18,
1025 14327–14350, doi: [10.5194/acp-18-14327-2018](https://doi.org/10.5194/acp-18-14327-2018), 2018.

1026

1027 Spek, A. L. J., Unal, C. M. H., Moisseev, C. N., Russchenberg, H. W. J., Chandrasekar, V., Dufournet, Y.: A New Techniques
1028 to Categorize and Retrieve the Microphysical Properties of Ice Particles above the Melting Layer Using Radar Dual-
1029 Polarization Spectral Analysis, Jtech, doi: 10.1175/2007JTECHA944.1, 2008.

1030

1031 Stevens, B., Acquistapace, C., Hansen, A., Heinze, R., Klinger, C., Klocke, D., Schubotz, W., Windmiller, J., Adamidis, P.,
1032 Arka, I., Barlakas, V., Biercamp, J., Brueck, M., Brune, S., Buehler, S., Burkhardt, U., Cioni, G., Costa-Surós, M., Crewell,
1033 S., Crueger, T., Deneke, H., Friederichs, P., Carbajal Henken, C., Hohenegger, C., Jacob, M., Jakub, F., Kalthoff, N., Köhler,
1034 M., Van Laar, T. W., Li, P., Löhnert, U., Macke, A., Madenach, N., Mayer, B., Nam, C., Naumann, A. K., Peters, K., Poll, S.
1035 , Quaas, J., Röber, N., Rochetin, N., Rybka, H., Scheck, L., Schemann, V., Schnitt, S., Seifert, A., Senf, F., Shapkalijevski,
1036 M., Simmer, C., Singh, S., Sourdeval, O., Spickermann, D., Strandgren, J., Tessiot, O., Vercauteren, N., Vial, J., Voigt, A.,
1037 and Zängl, G.: Large-eddy and storm resolving models for climate prediction - the added value for clouds and precipitation, J.
1038 Meteorol. Soc. Japan, 98, doi:10.2151/jmsj. 2020-021, 2020.

1039

1040 Stevens, B., et al.: Atmospheric component of the MPI-M Earth System Model: ECHAM6, *J. Adv. Model. Earth Syst.* 5: 146–
1041 172, doi: 10.1002/jame.20015, 2013.

1042

1043 Stevens, B. and Feingold, G.: Untangling Aerosol Effects on Clouds and Precipitation in a Buffered System, *Nature*, 461, 607–
1044 613, 2009.

1045

1046 Sundqvist, H., et al., Condensation and cloud parameterization studies with a mesoscale numerical weather prediction model,
1047 *Mon. Weather Rev.*, 117, 1641–1657, 1989.

1048

1049 Takahashi, T.: High ice crystal production in winter cumuli over the Japan Sea, *Geophysical research letters*, 20.6, 451–454,
1050 1993.

1051

1052 Takahashi, T., Yoshihiro N., and Yuzuru K.: Possible high ice particle production during graupel–graupel collisions, *J. Atmos.*
1053 *Sci.*, 52.24, 4523–4527, 1995.

1054

1055 Takahashi, T.: Influence of liquid water content and temperature on the form and growth of branched planar snow crystals in
1056 a cloud, *J. Atmos. Sci.*, 71.11, 4127–4142, 2014.

1057

1058 Tiedtke, M.: Representation of clouds in large scale models, *Mon. Weather Rev.*, 121, 3040–3061, 1993.

1059

1060 Tompkins, A.: A prognostic parameterization for the subgrid-scale variability of water vapor and clouds in large-scale models
1061 and its use to diagnose cloud cover, *J. Atmos. Sci.*, 59:1917–1942, 2002.

1062

1063 Trömel, S., Quaas, J., Crewell, S., Bott, A., and Simmer, C.: Polarimetric Radar Observations Meet Atmospheric Modelling.
1064 19th International Radar Symposium (IRS), Bonn, doi: 10.23919/IRS.2018.8448121, 2018.

1065

1066 Trömel, S., Ryzhkov, A. V., Hickman, B., Mühlbauer, K., and Simmer, C.: Polarimetric Radar Variables in the Layers of
1067 Melting and Dendritic Growth at X Band—Implications for a Nowcasting Strategy in Stratiform Rain, *J. Appl. Meteor.*
1068 *Climatol.*, 58, 2497–2522, doi:10.1175/JAMC-D-19-0056.1, 2019.

1069

1070 Trömel, S., A. V. Ryzhkov, P. Zhang, and C. Simmer: The microphysical information of backscatter differential phase δ in the
1071 melting layer, *J. Appl. Meteor. Climatol.*, 53, 2344–2359, 2014.

1072

1073 Verlinde, J., Rambukkange, M. P., Clothiaux, E. E., McFarquhar, G. M., and Eloranta, E. W.: Arctic multilayered, mixed-
1074 phase cloud processes revealed in millimeter-wave cloud radar Doppler spectra, *J. Geophys. Res. Atmos.*, 118, 13199–13213,
1075 doi: 10.1002/2013JD020183, 2013.

1076

1077 Vogl, T., Maahn, M., Kneifel, S., Schimmel, W., Moisseev, D., and Kalesse-Los, H.: Using artificial neural networks to predict
1078 riming from Doppler cloud radar observations, *Atmos. Meas. Tech. Discuss.* [preprint], <https://doi.org/10.5194/amt-2021-137>,
1079 in review, 2021.

1080

1081 Voigt, C., Schumann, U., Jurkat, T., Schäuble, D., Schlager, H., Petzold, A., Gayet, J.-F., Krämer, M., Schneider, J., Borrmann,
1082 S., Schmale, J., Jessberger, P., Hamburger, T., Lichtenstern, M., Scheibe, M., Gourbeyre, C., Meyer, J., Kübbeler, M., Frey,
1083 W., Kalesse, H., Butler, T., Lawrence, M. G., Holzäpfel, F., Arnold, F., Wendisch, M., Döpelheuer, A., Gottschaldt, K.,
1084 Baumann, R., Zöger, M., Sölch, I., Rautenhaus, M., and Dörnbrack, A.: In-situ observations of young contrails – overview
1085 and selected results from the CONCERT campaign, *Atmos. Chem. Phys.*, 10, 9039–9056, doi:10.5194/acp-10-9039-2010,
1086 2010.

1087

1088 Voigt, C., Jeßberger, P., Jurkat, T., Kaufmann, S., Baumann, R., Schlager, H., Bobrowski, N., Guffirda, G., and Salerno, G.:
1089 Evolution of CO₂, SO₂, HCl and HNO₃ in the volcanic plumes from Etna, *Geophys. Res. Lett.*, 41,
1090 doi:10.1002/2013GL058974, 2014.

1091

1092 Voigt, C., Schumann, U., Minikin, A., Abdelmonem, A., Afchine, A., Borrmann, S., Boettcher, M., Buchholz, B., Bugliaro,
1093 L., Costa, A., Curtius, J., Dollner, M., Dörnbrack, A., Dreiling, V., Ebert, V., Ehrlich, A., Fix, A., Forster, L., Frank, F.,
1094 Fütterer, D., Giez, A., Graf, K., Groß, J., Groß, S., Heimerl, K., Heinold, B., Hüneke, T., Järvinen, E., Jurkat, T., Kaufmann,
1095 S., Kenntner, M., Klingebiel, M., Klimach, T., Kohl, R., Krämer, M., Krisna, T. C., Luebke, A., Mayer, B., Mertens, S.,
1096 Molleker, S., Petzold, A., Pfeilsticker, K., Port, M., Rapp, M., Reutter, P., Rolf, C., Rose, D., Sauer, D., Schäfler, A., Schlage,
1097 R., Schnaiter, M., Schneider, J., Spelten, N., Spichtinger, P., Stock, P., Walser, A., Weigel, R., Weinzierl, B., Wendisch, M.,
1098 Werner, F., Wernli, H., Wirth, M., Zahn, A., Ziereis, H., and Zöger, M.; ML-CIRRUS: The Airborne Experiment on Natural
1099 Cirrus and Contrail Cirrus with the High-Altitude Long-Range Research Aircraft HALO, *B. Am. Meteorol. Soc.* 98(2), 271-
1100 288, doi:[bams-d-15-00213.1](https://doi.org/10.1175/BAMS-D-15-00213.1), 2017.

1101 Voigt, C., Lelieveld, J., Schlager, H., Schneider, J., Sauer, D., Meerkötter, R., Pöhlker, M., Bugliaro, L., Curtius, J.,
1102 Erbertseder, T., Hahn, V., Jöckel, P., Li, Q., Marsing, A., Mertens, M., Pöhlker, C., Pöschl, U., Pozzer, A., Tomsche, L., and
1103 Schumann, U.: Aerosol and Cloud Changes during the Corona Lockdown in 2020 - First highlights from the BLUESKY
1104 campaign; EGU21-13134, <https://meetingorganizer.copernicus.org/EGU21/session/40818>, 2021.

1105 Wang, M., Zhao, K., Pan, Y., Xue, M.: Evaluation of simulated drop size distributions and microphysical processes using
1106 polarimetric radar observations for landfalling Typhoon Matmo (2014), *J. Geophys. Res. Atmos.*, 125, 1-20,
1107 doi:10.1029/2019JD031527, 2020.

1108 Weissmann, M., M. Göber, C. Hohenegger, T. Janjic, J. Keller, C. Ohlwein, A. Seifert, S. Trömel, T. Ulbrich, K. Wapler, C.
1109 Bollmeyer, H. Deneke: The Hans-Ertel Centre for Weather Research – Research objectives and highlights from its first three
1110 years. *Meteorol. Z.*, 23(3), 193 – 208, 2014.

1111 Wendisch, M., Pöschl, U., Andreae, M. O., Machado, L. A. T., Albrecht, R., Schlager, H., Rosenfeld, D., Martin, S. T.,
1112 Abdelmonem, A., Afchine, A., Araùjo, A. C., Artaxo, P., Aufmhoff, H., Barbosa, H. M. J., Borrmann, S., Braga, R., Buchholz,
1113 B., Cecchini, M. A., Costa, A., Curtius, J., Dollner, M., Dorf, M., Dreiling, V., Ebert, V., Ehrlich, A., Ewald, F., Fisch, G.,
1114 Fix, A., Frank, F., Fütterer, D., Heckl, C., Heidelberg, F., Hüneke, T., Jäkel, E., Järvinen, E., Jurkat, T., Kanter, S., Kästner,
1115 U., Kenntner, M., Kesselmeier, J., Klimach, T., Knecht, M., Kohl, R., Kölling, T., Krämer, M., Krüger, M., Krisna, T. C.,
1116 Lavric, J. V., Longo, K., Mahnke, C., Manzi, A. O., Mayer, B., Mertes, S., Minikin, A., Molleker, S., Münch, S., Nillius, B.,
1117 Pfeilsticker, K., Pöhlker, C., Roiger, A., Rose, D., Rosenow, D., Sauer, D., Schnaiter, M., Schneider, J., Schulz, C., de Souza,
1118 R. A. F., Spanu, A., Stock, P., Vila, D., Voigt, C., Walser, A., Walter, D., Weigel, R., Weinzierl, B., Werner, F., Yamasoe, M.
1119 A., Ziereis, H., Zinner, T., and Zöger, M.: ACRIDICON–CHUVA Campaign: Studying Tropical Deep Convective Clouds and
1120 Precipitation over Amazonia Using the New German Research Aircraft HALO, *B. Am. Meteorol. Soc.*, 97(10), 1885-1908,
1121 doi:[bams-d-14-00255.1](https://doi.org/10.1175/bams-d-14-00255.1), 2016.

1122 Wolfensberger, D. and Berne, A.: From model to radar variables: a new forward polarimetric radar operator for COSMO,
1123 *Atmos. Meas. Tech.*, 11, 3883-3916, doi: 10.5194/amt-11-3883-2018, 2018.

1124 Xie, X., Evaristo, R., Trömel, S., Saavedra, P., Simmer, C., and Ryzhkov, A.: Radar Observation of Evaporation and
1125 Implications for Quantitative Precipitation and Cooling Rate Estimation, *J. Atmos. Oceanic Technol.* 33(8), 1779-1792,
1126 doi:10.1175/JTECH-D-15-0244.1, 2016.

1127

1128 Xie, X., Shrestha, P., Mendrok, J., Carlin, J., Trömel, S., and Blahak, U.: Bonn Polarimetric Radar forward Operator (B-PRO),
1129 CRC/TR32 Database (TR32DB), doi:10.5880/TR32DB.41, 2021, (accessed 8 April 2021).

1130

1131 Xue, L., Fan, J., Lebo, Z. J., Wu, W., Morrison, H., Grabowski, W. W., Chu, X., Geresdi, I., North, K., Stenz, R., Gao, Y.,
1132 Lou, X., Bansemer, A., Heymsfield, A. J., McFarquhar, G. M., and Rasmussen, R. M.: Idealized Simulations of a Squall Line
1133 from the MC3E Field Campaign Applying Three Bin Microphysics Schemes: Dynamic and Thermodynamic Structure,
1134 *Monthly Weather Review*, 145(12), 4789-4812, doi:10.1175/MWR-D-16-0385.1, 2017.

1135

1136 You, C.-R., Chung, K.-S., and Tsai, C.-C.: Evaluating the performance of convection-permitting model by using dual-
1137 polarimetric radar parameters: Case study of SoWMEX IOP8, *Remote Sensing*, 12(18):3004, 1-25, doi:10.3390/rs12183004,
1138 2020.

1139

1140 Zängl, G., et al.: The ICON (icosahedral non-hydrostatic) modelling framework of DWD and MPI-M: Description of the non-
1141 hydrostatic dynamical core, *Q. J. Roy. Meteor. Soc.*, 141, 563–579, 2015.

1142

1143 Zeng, Y., Janjic, T., Lozar, A. de, Welzbacher, C. A., Blahak, U., and Seifert, A.: Assimilating radar radial wind and reflectivity
1144 data in an idealized setup of the COSMO-KENDA system, *Atmospheric Research*, 249, 105282,
1145 [doi:10.1016/j.atmosres.2020.105282](https://doi.org/10.1016/j.atmosres.2020.105282), 2021a.

1146

1147 Zeng, Y., Janjic, T., Feng, Y., Blahak, U., de Lozar, A., Bauernschubert, E., Stephan, K., and Min, J.: Interpreting estimated
1148 observation error statistics of weather radar measurements using the ICON-LAM-KENDA system, *Atmos. Meas. Tech.*, 14,
1149 5735–5756, <https://doi.org/10.5194/amt-14-5735-2021>, 2021b.

1150

1151 Zeng, Y., Janjic, T., Lozar, A. de, Rasp, S., Blahak, U., Seifert, A., and Craig, G. C.: Comparison of methods accounting for
1152 subgrid-scale model error in convective-scale data assimilation, *Mon. Wea. Rev.*, 148, 2457-2477, 2020.

1153

1154 Zeng Y., Janjic, T., Sommer, M., Lozar, A. de, Blahak, U., and Seifert, A.: Representation of model error in convective-scale
1155 data assimilation: additive noise based on model truncation error, *J. Adv. Model. Earth Sy.*, 11, 752-770, 2019.

1156

1157 Zeng, Y., Janjic, T., Lozar, A. de, Blahak, U., Reich, H., Keil, C., and Seifert, A.: Representation of model error in convective-
1158 scale data assimilation: Additive noise, relaxation methods and combinations, *J. Adv. Model. Earth Sy.*, 10, 2889–2911, 2018.

1159

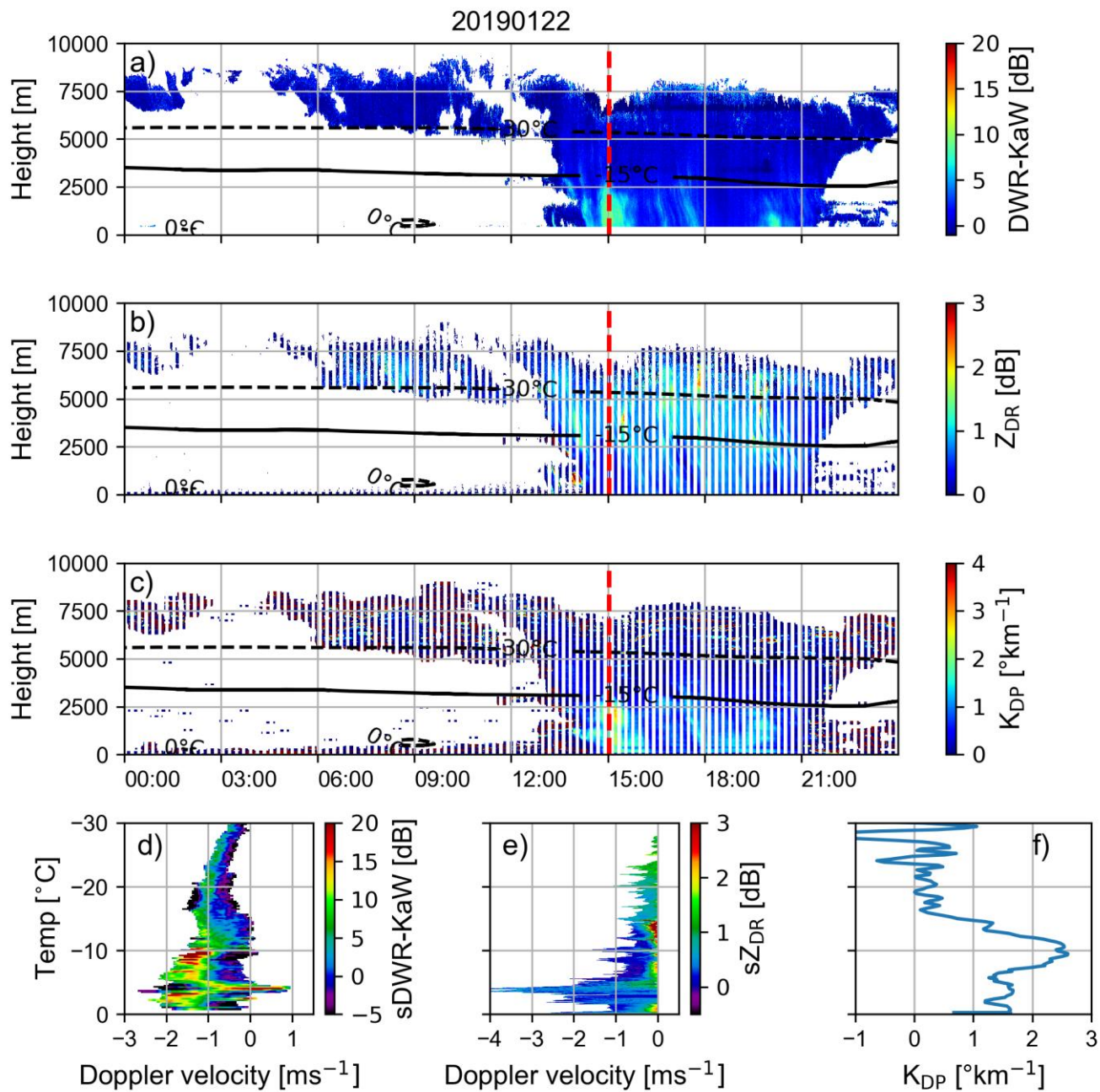
1160 Zeng, Y., Blahak, U., and Jerger, D.: An efficient modular volume-scanning radar forward operator for NWP models:
1161 description and coupling to the COSMO model, *Q. J. Roy. Meteor. Soc.*, 142(701), 3234-3256, 2016

1162

1163 Zhu, K., Xue, M., Ouyang, K., and Jung, Y.: Assimilating polarimetric radar data with an ensemble Kalman filter: OSSEs with
1164 a tornadic supercell storm simulated with a two-moment microphysics scheme, *Q. J. Roy. Meteor. Soc.*, 146: 1880– 1900,
1165 [doi:10.1002/qj.3772](https://doi.org/10.1002/qj.3772), 2020.

1166

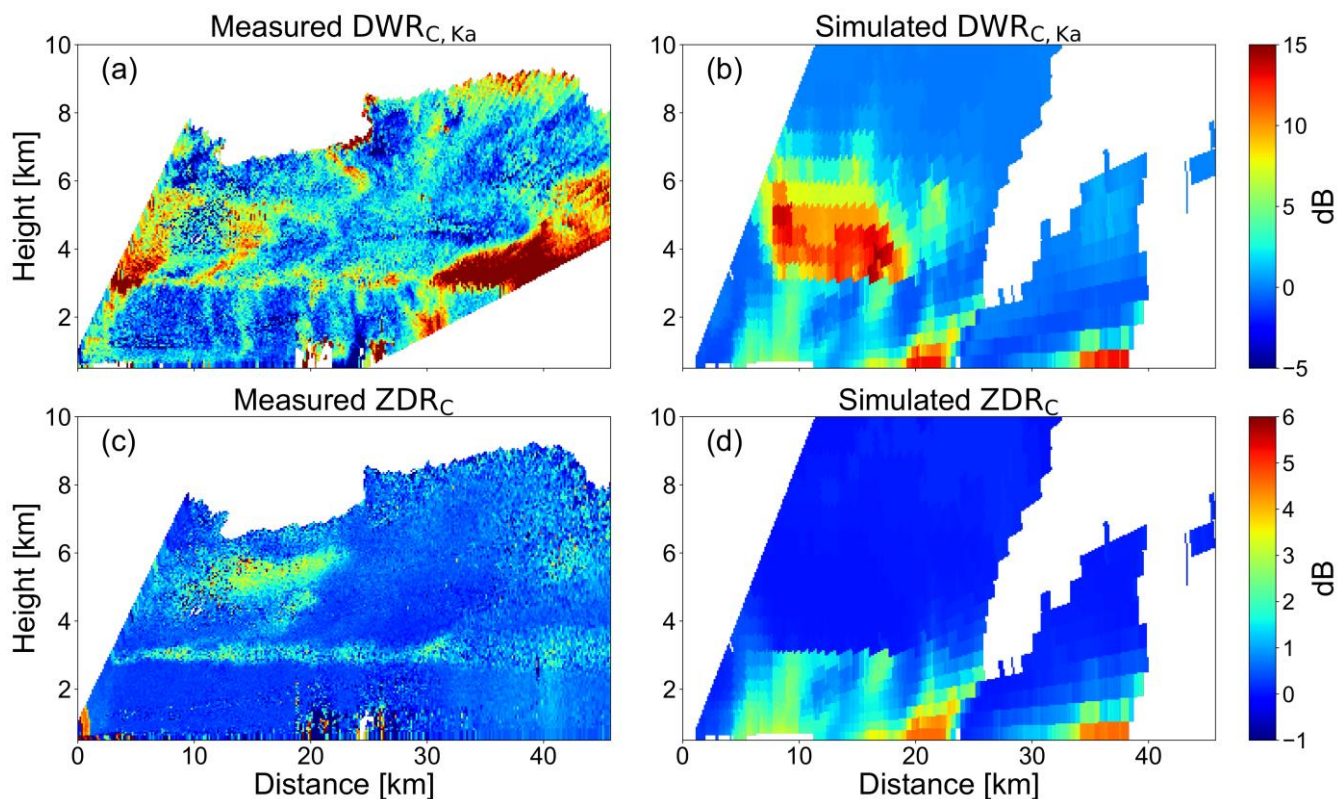
1167



1168
 1169 **Figure 1: Observations at JOYCE-CF shows a) DWRKaW, b) Z_{DR} (measured at a 30° elevation angle), c) K_{DP} (also measured at 30°**
 1170 **elevation angle) on 22 January 2019. Panels d)-f) show the observed DWR-spectrum, Z_{DR}-spectrum and K_{DP}-profile at 15:00 UTC**
 1171 **(indicated by the red line in panels a)-c))**

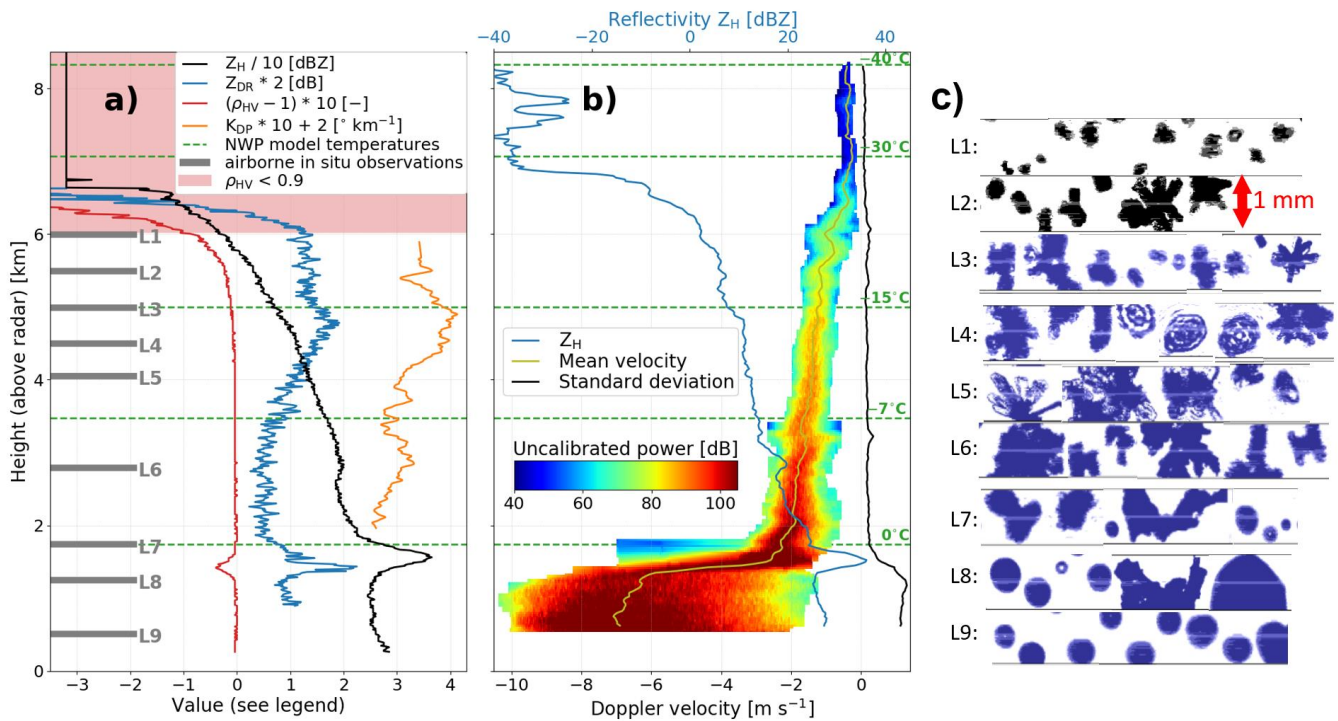
1174

1175

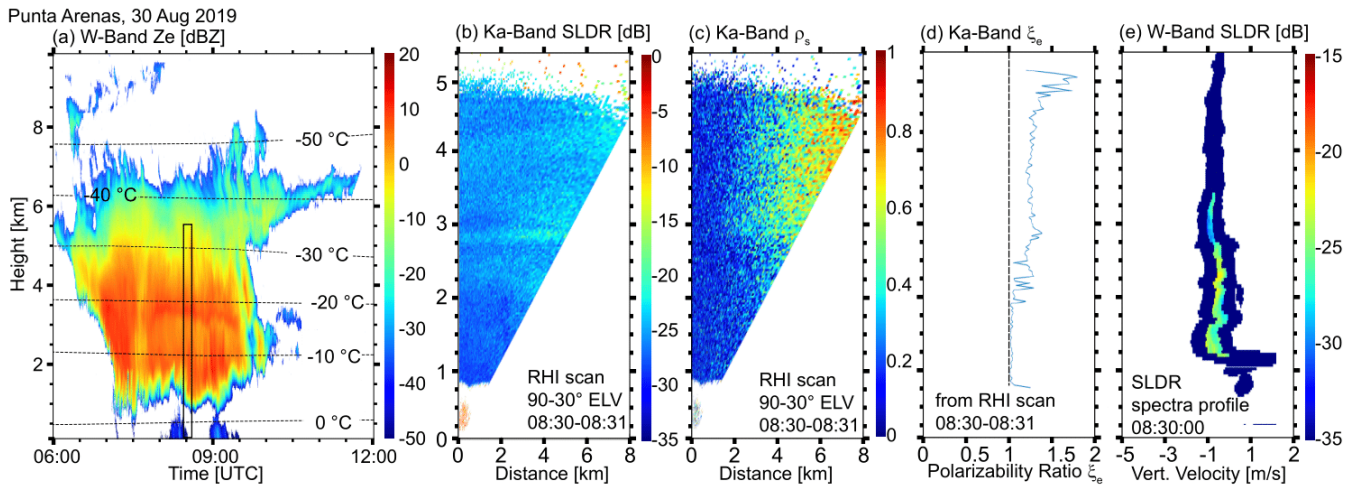


1176

1177 **Figure 2:** (a) Dual-wavelength ratio between the C-band POLDIRAD and Ka-band miraMACS measurements on the 7th July 2019,
1178 (b) simulated dual-wavelength ratio, (c) differential radar reflectivity Z_{DR} measured by the C-band radar POLDIRAD, and (d)
1179 simulated Z_{DR} of a comparable, but not identical, precipitation event using the P3 scheme (Morrison and Milbrandt, 2015).

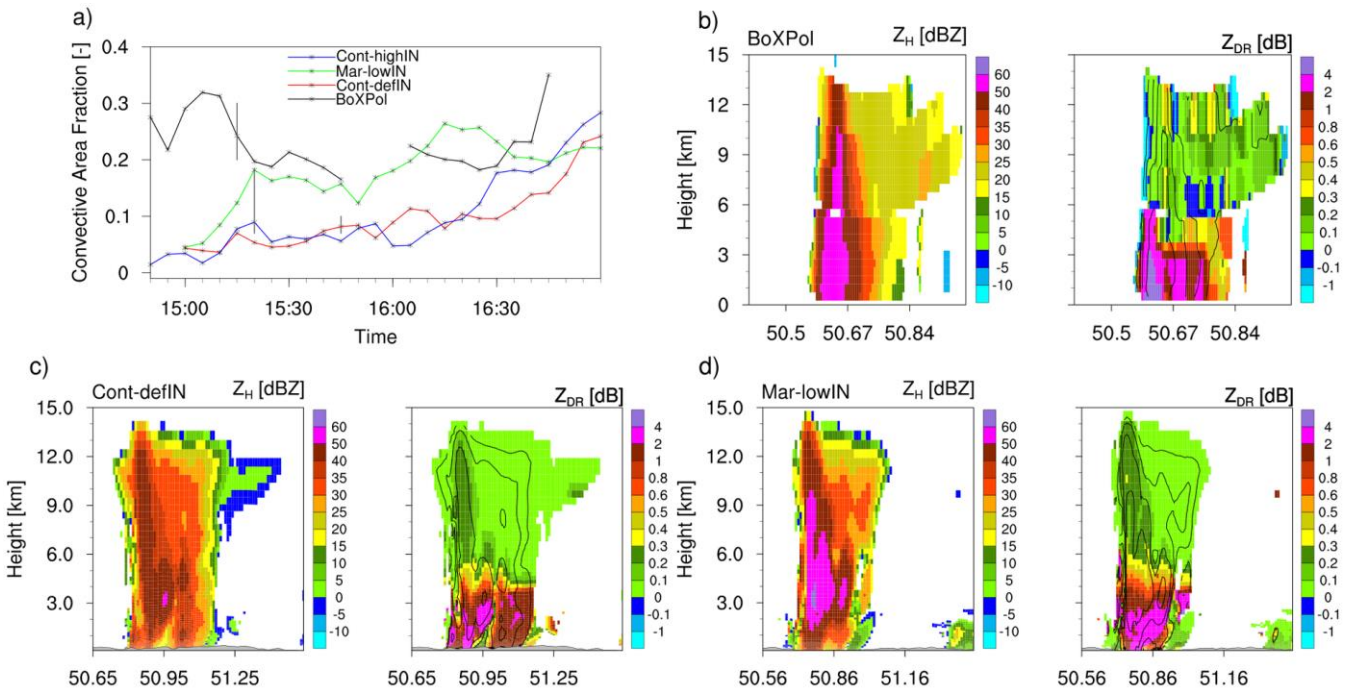


1180
 1181 **Figure 3: Measurements of slant-viewing and zenith-pointing polarimetric C-band weather radar scans with NWP model based**
 1182 **temperature levels and airborne in-situ observations: (a) quasi-vertical profiles (QVPs) of radar reflectivity Z_H , differential**
 1183 **reflectivity Z_{DR} , copolar cross-channel correlation coefficient ρ_{HV} , and the specific differential phase K_{DP} estimated from (noisy)**
 1184 **measurements of the differential phase by aggressive filtering above the melting layer; (b) average Doppler spectra from a 15 s**
 1185 **birdbath scan and corresponding first 3 moments at each radar bin height: reflectivity, power-weighted mean velocity and standard**
 1186 **deviation; (c) in situ particle images (downward-looking projection images) collected at altitudes L1 to L9.**



1191
1192
1193
1194
1195
1196
1197

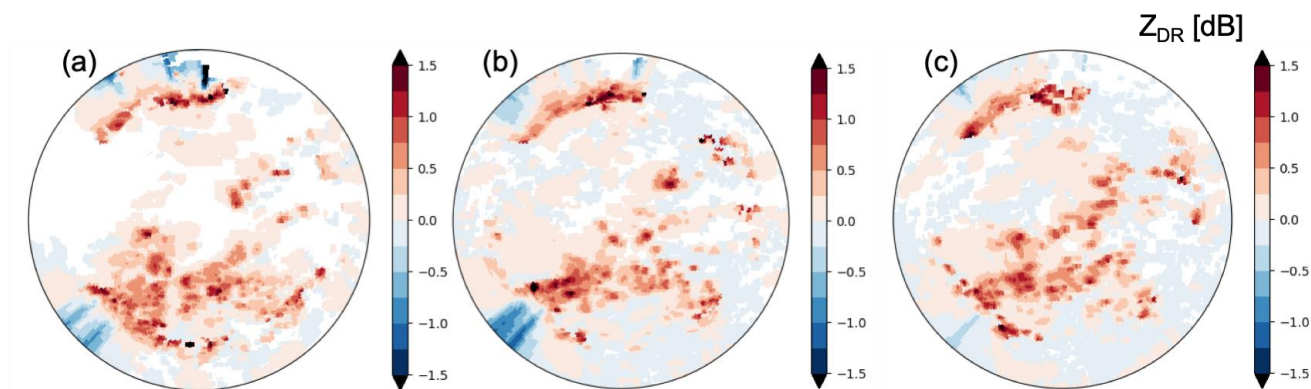
Figure 4: Case study of a deep mixed-phase cloud event observed with multiwavelength polarimetric cloud radars at Punta Arenas, Chile, on 30 August 2019. (a) vertical-pointing W-Band (94-GHz) radar reflectivity factor Z_e and isolines of modeled air temperature, (b) and (c) Ka-Band (35-GHz) RHI scans (90°-30° elevation) of slanted linear depolarization ratio SLDR and co-cross correlation coefficient in the slanted basis ρ_s , respectively, from 08:30-08:31 UTC, (d) profile of the shape index polarizability ratio (ξ_e) obtained from the RHI scans shown in (b) and (c), and (e) height spectrogram (at 90° elevation) of W-Band SLDR from 08:30:00 UTC. The time and height frame of panels (b-e) is indicated by the black rectangle in (a).



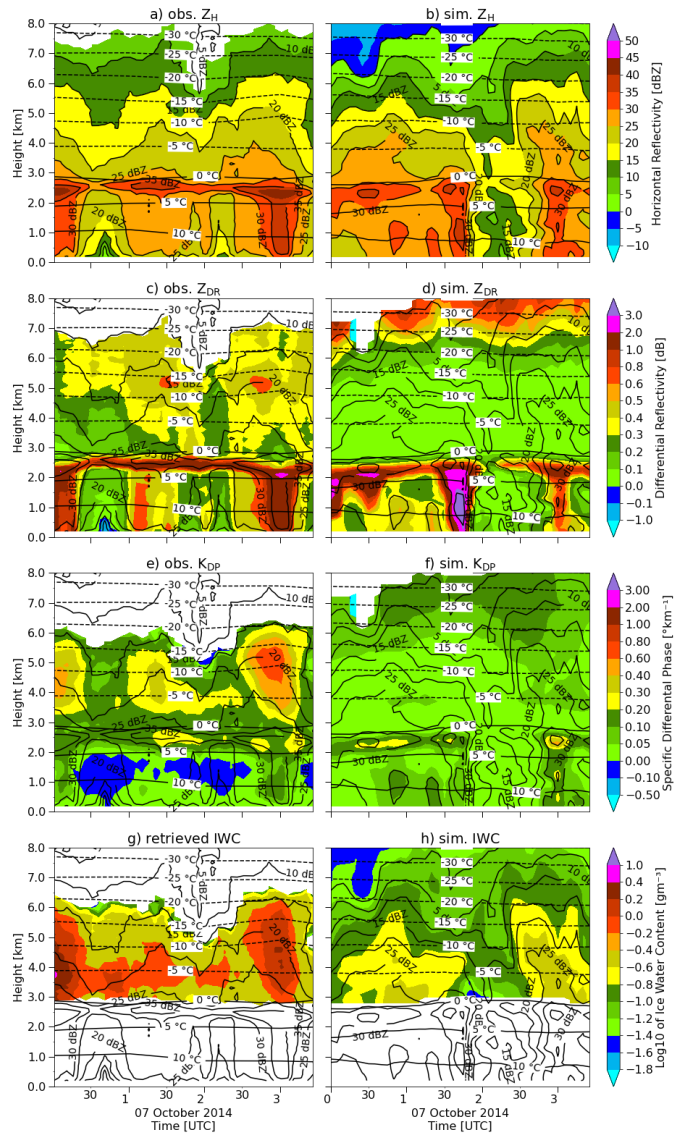
1198
1199

1200 **Figure 5: Time-series of Convective Area Fraction (CAF) evolution (panel a) and reconstructed observed (panel b) and**
1201 **simulated/synthetic range-height-indicators (RHI) of horizontal reflectivity Z_H and differential reflectivity Z_{DR} (panels c and d).**
1202 **Synthetic RHIs are based on simulations for actual land-cover with different perturbations of CN and IN concentrations, where**
1203 **Cont-defIN indicates continental aerosol with default IN concentration and Mar-lowIN indicates maritime aerosol with low IN**
1204 **concentration. The gaps in the BoXPol-observed CAF time series are due to strong attenuation. The vertical grey bars (panel a)**
1205 **indicate the times at which the RHIs are compared.**

1206



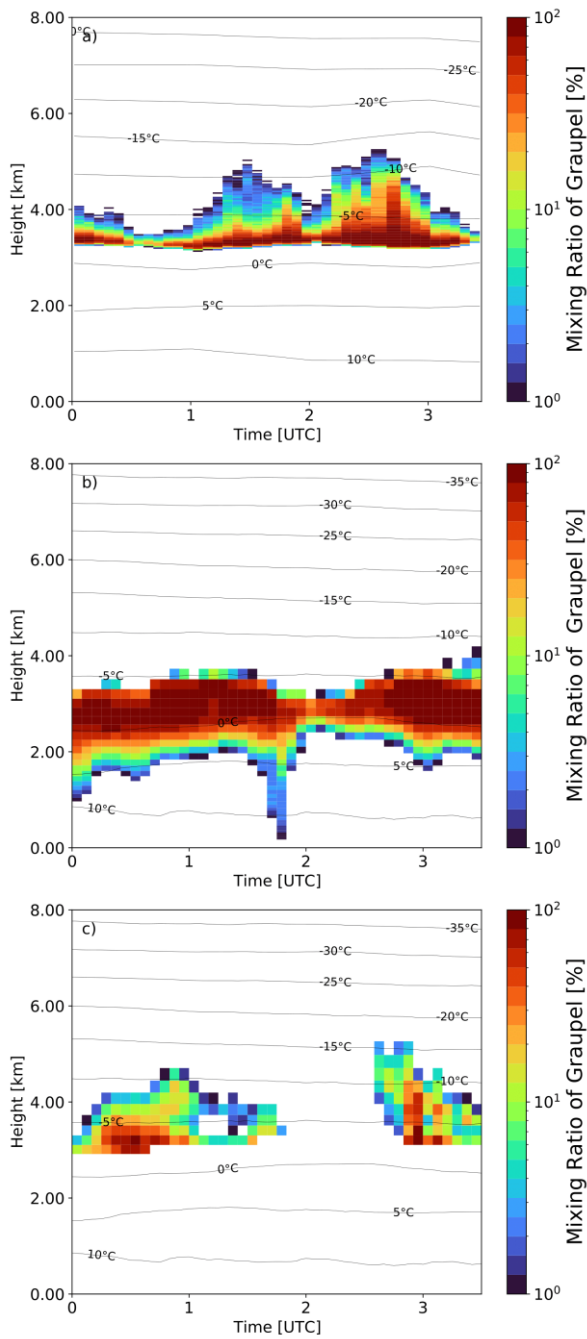
1208 **Figure 6: Synthetic PPI of Z_{DR} at 0.5 deg elevation for the DWD radar site Neuheilenbach based on the analysis obtained for June**
1209 **4 at 16:00 UTC by assimilation of radar reflectivity and using three different ways to specify the model error: large scale uncertainty**
1210 **(panel a), large plus unresolved scales uncertainty (panel b) and in addition the use of the warm bubble approach (panel c).**



1211

1212 **Figure 7: Quasi-vertical profiles (QVPs) of observed (left column) and simulated (right column) polarimetric radar variables**
 1213 **horizontal reflectivity Z_H (panels a and b), differential reflectivity Z_{DR} (panels c and d), specific differential phase K_{DP} (panels e and**
 1214 **f), together with radar-retrieved (panel g) and simulated ice water content (IWC, panel h). The QVPs show a stratiform rain event**
 1215 **observed on 7 October 2014 between 0:00 and 3:30 UTC with the polarimetric X-band radar in Bonn, BoXPol, and simulated with**
 1216 **COSMO version 5.1 and the 2-moment cloud microphysics scheme.**

1217



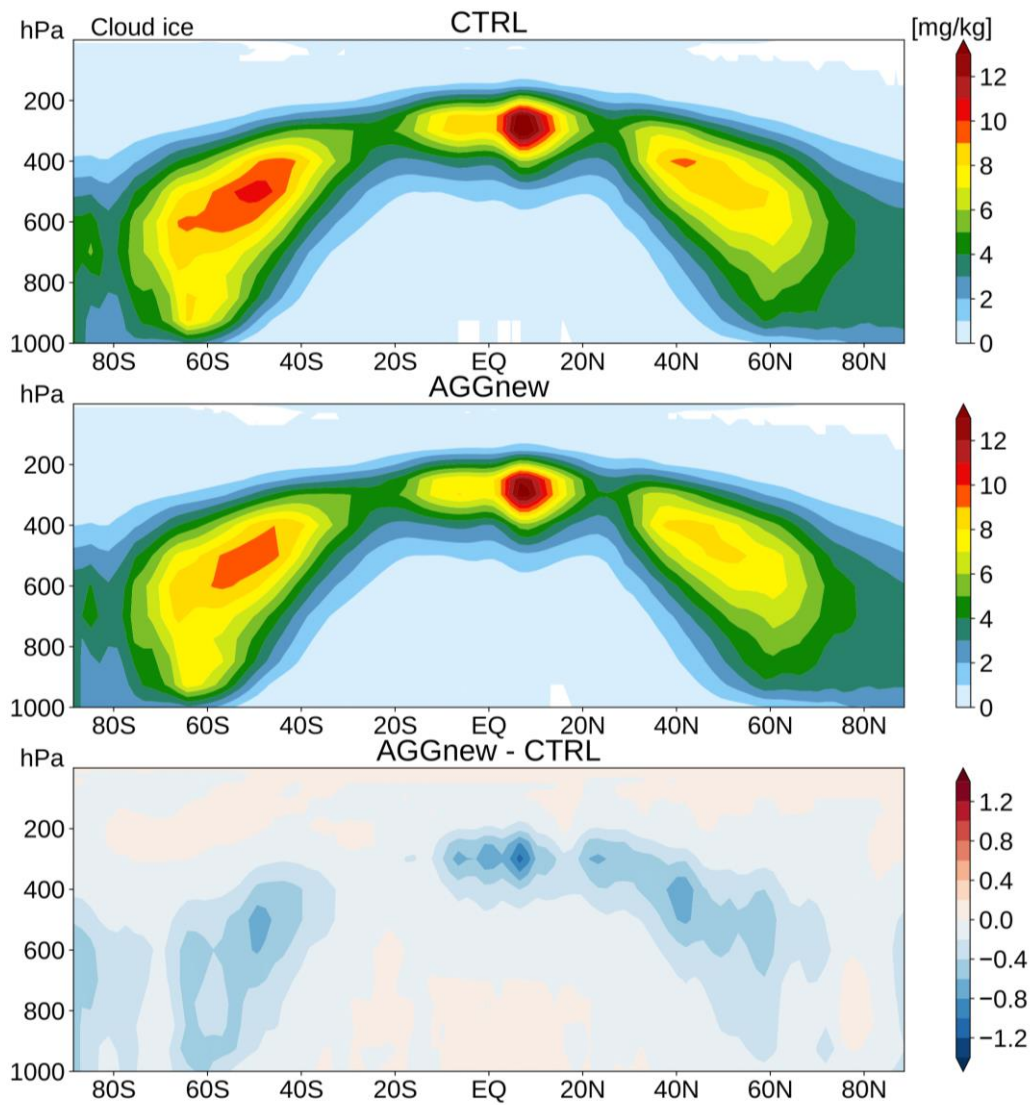
1218

1219 **Figure 8:** Retrieved and simulated graupel mixing ratios, defined as the percentage of graupel in the total hydrometeor mass, for
 1220 the stratiform rain event shown in Fig. 7 (7 October 2014, 0:00-3:30 UTC). An advanced hydrometeor classification and
 1221 quantification algorithm has been applied to polarimetric BoXPOL measurement (panel a) and to simulated radar variables based
 1222 on COSMO simulations (panel c) and compared to the COSMO-simulated graupel mixing (panel b).

1223

1224

1225



CTRL – control run

AGGnew – run with the stochastic aggregation scheme

1226

1227 **Figure 9: Specific ice water, q_i , [g kg⁻¹] as zonal, annual mean for (top) standard ICON GCM output, (middle) aggregation**
1228 **parameterization revised as stochastic parameterization drawing from the q_i subgrid-variability PDF, and (bottom) difference**
1229 **between the two.**

1230

1231

1232

1233

1234